Local Earthquake Tomography at Mount Pinatubo, Philippines

Jake Beale

Thesis submitted to the Faculty of the
Virginia Polytechnic Institute and State University
in partial fulfillment of the
requirements for the degree of

Master of Science
in
Geophysics

Dr. John Hole, Chair

Dr. Martin Chapman

Dr. Arthur Snoke

August 9, 2004
Blacksburg, Virginia

Keywords: Earthquake Tomography, 3-D Velocity Model, Volcano, Low Velocity Zone

Local Earthquake Tomography at Mount Pinatubo, Philippines

Jake Beale

Abstract

A new high-resolution 3-dimensional P-wave velocity model for Mt. Pinatubo volcano was developed by tomographic inversion of P-wave arrivals from 3,007 earthquakes recorded during a four month period from May to August, 1991. The arrivals were recorded by a network of seismic stations, consisting of seven pre-eruption stations and seven post-eruption stations. Two stations survived the June eruptions. First-arrival travel times were calculated using a finite-difference solution to the eikonal equation. An iterative, linearized approximation of the nonlinear tomography problem was used to solve separately for both velocity structure and hypocenter locations. Several inversions performed with different initial parameters and convergence schemes, and synthetic checkerboard reconstructions indicate a horizontal spatial resolution of velocity perturbations near 4 km. However, the network sparseness allows for a substantial trade-off between focal depth, origin time, and the vertical velocity profile. Many hypocenter clusters collapse from diffuse clouds into tighter features after 3-D relocation. These bands of earthquakes appear to represent fault-related structures. Three low-velocity (relative to the horizontal average) anomalies exist within the well-resolved portion of the velocity model. These anomalies are spatially associated with pre- and post-eruption earthquakes oriented along mapped surface fault zones. Similar anomalies observed at different volcanoes have been previously interpreted as magma related. The low-velocity anomalies at Pinatubo are interpreted as highly fractured, hot volumes of mostly competent rock, which may contain partial melt.

Acknowledgements

Thanks to all who have aided me during the completion of this research. Dr. Jim Mori provided useful insights into the details of his work at Pinatubo. Dr. John Power has offered continued advice regarding the earthquake data from the eruption. Dr. Harley Benz provided the arrival time data used in this research. Figures were (at least in part) made using GMT. The committee members listed above have, of course, put forth their effort and time and for that I thank them. Thanks to the staff of the Department of Geosciences, they are the real catalyst behind all of our efforts. Also, thanks to the faculty of the Department of Geosciences, and to the students that I have known while here at Virginia Tech. I am very grateful, and fortunate, to have been at this department during the tenure of our long-serving Chair, Dr. Cahit Coruh. His service to our department has certainly benefited me both personally and professionally. Without the support of my family and friends, I would probably have given up long ago. Thanks Mom! Thank you all and God bless you.

Table of Contents

Index of Figures

Index of Tables

Introduction

Volcanic eruptions present a significant threat to human safety and society. Both the scenic beauty of the terrain and the surrounding fertile soils attract large populations of humans to settle areas near volcanoes. Every year, many volcanoes around the world erupt, with some of these eruptions lasting several months or more. Despite the large number of eruptions, most are not highly destructive. However, there are volcanoes worldwide which are associated with destructive and often catastrophic eruptions. These eruptions take a high toll both in human life and in economic losses, such as property loss and the residual effects of a displaced population. Monitoring the activity of these explosive volcanoes is very important. While it is unreasonable to expect to prevent eruptions, reasonable judgements about the behavior of a developing eruption are necessary to reduce damage and loss of life.

Volcanic activity is associated with several tectonic settings. Volcanoes are found in extensional settings, such as mid-ocean rifts, and near mantle plumes, such as Hawaii, but the most destructive volcanoes are related to the subduction of oceanic plates, such as many of the volcanoes that make up the "Pacific Ring of Fire". The magmatic arcs found in subduction related settings are usually associated with explosive eruptions. The combination of the explosive nature of the eruptions and the tendency for human populations to reside near explosive volcanoes places a high priority on the understanding volcanic hazards.

There are many tools available to volcanic researchers today, including geologic investigations of the surrounding volcanic deposits, chemical analysis of local groundwater (especially hot springs), monitoring of volcanic steam and gas emissions, tracking of changing stress/strain fields, monitoring near-surface volume changes on the volcano, and monitoring the changes in the characteristics of recorded seismic activity. In order to fully understand the inner workings of the volcanic system, information from as many sources as possible must be integrated, with the ultimate goal being the ability to accurately forecast the size and timing of eruptions early enough for an organized evacuation of potentially affected areas.

One particular aspect that is vital to our understanding of the volcanic system is the structure of the magma conduit network. If this structure can be accurately resolved, it may be possible to track underground magma movements based on the timing and location of associated small earthquakes. Seismic tomography is a primary tool that is used to examine this structure and thereby improve hypocenter accuracy. Seismic tomography can be performed using either controlled explosions or natural seismic sources. In almost all cases involving volcanoes, the natural seismic unrest of the erupting volcano is utilized, the many small earthquakes acting as sources. This is often referred to as local earthquake tomography (LET).

Earthquake tomography can be used to estimate the seismic velocity structure of a volume from an inversion of earthquake arrival time data. The method is similar to controlled source tomography, with the exception that the source locations are an added unknown. Also, there is no control over the locations of the sources. This causes the results to be non-unique, because there exists a nonlinear trade-off between velocity structure and hypocenter location and origin time. In the early stages of technique development, inversion for velocity structure was conducted without adjusting hypocenters. Since initial hypocenters are generally located within a simple 1-D velocity model, this approach is obviously flawed. To correct this flawed approach, researchers developed a method of simultaneously inverting for velocity structure and hypocenters [*Aki et al.*, 1977]. This method is sometimes approximated by an iterative approach allowing one parameter to be fixed while the other is adjusted.

LET has been applied to several volcanoes, including Kilauea [*Thurber*, 1984; *Dawson et al.*, 1999], Redoubt [*Benz et al.*, 1996], St. Helens [*Lees and Crosson*, 1989; *Lees*, 1992], Etna [*Villaseñor et al.*, 1998], and Pinatubo [*Mori et al.*, 1996] to image the magma conduit structure beneath the respective volcanoes. Based on seismic observations, magma bodies beneath volcanoes are believed to be relatively small, on the order of a few kilometers horizontally [*Dawson et al.*, 1999 and *Mori et al.*, 1996]. Typically, the spatial resolution of volcano tomography studies is on the order of 5-10 km horizontally, there are some exceptions, such as *Lees* [1992] and *Benz et al.* [1996], who both report resolutions near 1-2 km, and *Dawson et al.* [1999] who reports resolution of 0.5 km. Resolution is strongly influenced by the station spacing and earthquake distribution within the study area. The resolutions reported above correspond to the following approximate station spacings: [*Lees and Crosson*, 1989] 8-10 km; [*Villaseñor et al.*, 1998] 5 km; [*Mori et al.*, 1996] 10-20 km; [*Lees*, 1992] 0.5-5 km; [*Benz et al.*, 1996] 2 km; [*Dawson et al.*, 1999] 0.5 km. Spatial resolution on the order of a kilometer or larger increase the difficulty of making reasonable interpretations about magma conduit structure. Improved resolution and accurate hypocenters are essential for correlating seismic activity to subsurface structures and magma propagation [e.g. *Jones et al.*, 2001].

Mori et al. [1996] conducted three-dimensional seismic tomography using a subset of the arrival time data, 298 events out of thousands recorded, and the damped least-squares inversion code of *Eberhart-Phillips* [1993]. They inverted the arrival times for the three-dimensional velocity structure within an approximate 20 x 20 km area surrounding the summit of Mt. Pinatubo. The resulting velocity model contained a 4 to 5 km wide low velocity body below the summit of Pinatubo at depths between 6 and 11 km below sea level (b.s.l.), which they interpreted to be a large magma chamber that may have fed the 1991 eruptions [*Mori et al.*, 1996]. They also relocated the complete set of local hypocenters recorded from May to August in the three-dimensional velocity model and compared the distribution to the same hypocenters relocated using the initial one-dimensional velocity model. The hypocenters relocated using the three-dimensional velocity model are more tightly clustered and seem to show more of a spatial pattern suggestive of a magma conduit than those located within the one-dimensional velocity model [*Mori et al.*, 1996]. The apparently improved hypocenter locations were interpreted as an indication of an improved velocity model by *Mori et al.* 1996. Their velocity model was parameterized at 1 km spacings horizontally near the center of the model and 3 km near the outer edges [*Mori et al.*, 1996]. The method of *Michelini and McEvilly* [1991] was used to estimate the model parameter resolution at each of the grid nodes within the model. The results show that the model was generally well-parameterized within the volume of interest with respect to the amount of ray coverage utilized in the study. No tests of spatial resolution were conducted by *Mori et al.* [1996, and pers. comm. 2002]. (The issue of model parameter resolution vs. spatial resolution is addressed below.)

In the present study, the inversion algorithm of *Hole* [1992] modified by *Hole et al.* [2000] is used to quasi-simultaneously solve for hypocenter locations and invert for the three-dimensional velocity structure of the volume beneath Mt. Pinatubo. A large subset of the earthquake arrival time data from the 1991 eruptive period, including only the higher quality locations, is used in the inversion. These earthquakes are chronologically divided into pre-eruption and post-eruption groups. (However, all were used simultaneously in the present inversion.) The pre-eruption hypocenters are located within two shallow (< 8 km b.s.l.) clusters. The shallower of the two clusters lies roughly below the Pinatubo summit, and is spatially and temporally associated with the growth of a lava dome on the northwest flank of the summit

[*Harlow et al.*, 1996]. The other, larger cluster is slightly deeper and lies to the northwest of the summit. This cluster is spatially associated with the small caldera that formed during the June 15, 1991 eruption. The post-eruption earthquakes (which number about 4 times the amount of the pre-eruption events) consist of several clusters, as well many apparently randomly located events. The large scale patterns of these earthquake clusters have been established and are well documented by the group of researchers involved in the 1991 eruption response team.

The hypocenters used here include some earthquakes from the study of *Mori et al.* [1996] and many more which were not included in that study. The goal of repeating the tomography at Mt. Pinatubo is to produce a well-sampled, high-resolution velocity model, and to quantify that resolution, by using a different inversion algorithm and a more complete set of earthquake data. The resulting velocity model and hypocenters are presented and interpreted in terms of magma migration at Pinatubo.

Geologic Setting

Mt. Pinatubo is located on the island of Luzon, Philippines, about 75 km north of the capital city of Manila (Figure 1). Only two notable geologic investigations have been undertaken at Mt. Pinatubo. A geothermal exploration program was begun in 1982, with the goal of developing new electric power sources for the island of Luzon. The study was abandoned in 1990 after deep exploratory drilling produced discouraging results [*Delfin et al.*, 1996]. Soon after the study was abandoned, Pinatubo showed signs of renewed volcanic activity. During the early stages of the eruptions in June 1991, a group of U.S. Geological Survey (USGS) scientists was called to Pinatubo to assess the geologic hazards. The following description is based upon publications from those hasty investigations.

Pinatubo is part of the Luzon Volcanic Arc, which is the result of subduction of the South China Sea Plate beneath the Philippines Plate [*Bautista et al.*, 1996]. The volcano lies between the Eocene age Zambales Ophiolite Complex to the west and the late Miocene to Pliocene marine, nonmarine, and volcaniclastic sediments of the Tarlac Formation to the east, south and north [*Newhall et al.*, 1996; Figure 2]. Geothermal exploration wells drilled in the vicinity of the Pinatubo summit indicate that the rocks of the Zambales Ophiolite Complex underlie the Luzon Arc at Mt. Pinatubo [*Delfin et al.*, 1996].

There are two major orientations of faults and fractures intersecting at Mt. Pinatubo. The most dominant group consists of predominantly northwest- and north-trending dip slip faults with noticeable offset [*Delfin et al.*, 1996]. These fractures are aligned with the Iba Fracture Zone [*de Boer et al.,* 1980] (Figure 2), which cuts the Zambales Ophiolite and manifests itself at Pinatubo as the Maraunot and Dagsa faults as well as northwest-southeast trending surface hydrothermal discharges [*Delfin et al.*, 1996]. A separate group of northeast- and east-trending fractures intersect the Iba Fracture Zone at the south flank of the Pinatubo summit. These features, termed the Sacobia Lineament (Figure 2), are shorter with little apparent offset, but are well defined near the summit region [*Delfin et al.*, 1996].

There are two main groups of volcanic deposits from Mt. Pinatubo. Those belonging to an ancestral Pinatubo are dated at least 1 Ma, while younger deposits are included in the modern Pinatubo group [*Newhall et al.*, 1996]. There are several vents surrounding Pinatubo that were active just over 1 Mya, the approximate age of the giant caldera surrounding the modern Pinatubo [*Newhall et al.*, 1996] (Figure 2). Except for the immediate vicinity of Pinatubo's summit, all of the volcanic features surrounding Mt. Pinatubo have been eroded to the level of intrusive features (volcanic necks and plugs). All nearby volcanic centers have been inactive for over 1 Ma [*Newhall et al.*, 1996].

Based on the prior research at Mt. Pinatubo and observations of the 1991 eruptions, several particulars about Pinatubo are accepted within the community. Pinatubo is an active volcano that has experienced repeated, large eruptions for over 1 Ma [*Newhall et al.*, 1996]. The 1991 eruption appears to have been the result of hot, mafic magma rising from depths of 30 km or more and mixing (perhaps at depths of less than 10 km) with a cooler, dacitic magma body (probably partially solidified) [*Pallister et al.*, 1996 and *White*, 1996]. This mixing probably produced the intermediate magma that formed the andesite dome that appeared on the north face of Pinatubo just before the occurrence of major eruptions [*Pallister et al.*, 1996]. It is believed that this intermediate magma, being less dense and less viscous than the cooler dacitic magma above it, forced its way to the surface, creating a conduit for the cooler dacitic magma to reach the surface just days later [*Pallister et al.*, 1996 and *Endo et al.*, 1996]. Most of the above details were arrived at based upon geochemical and petrologic analysis of the June, 1991 erupted

materials. Refer to the volume "Fire and Mud" [*Newhall and Punongbayan*, 1996] for the complete details of studies related to the 1991 eruption of Mt. Pinatubo.

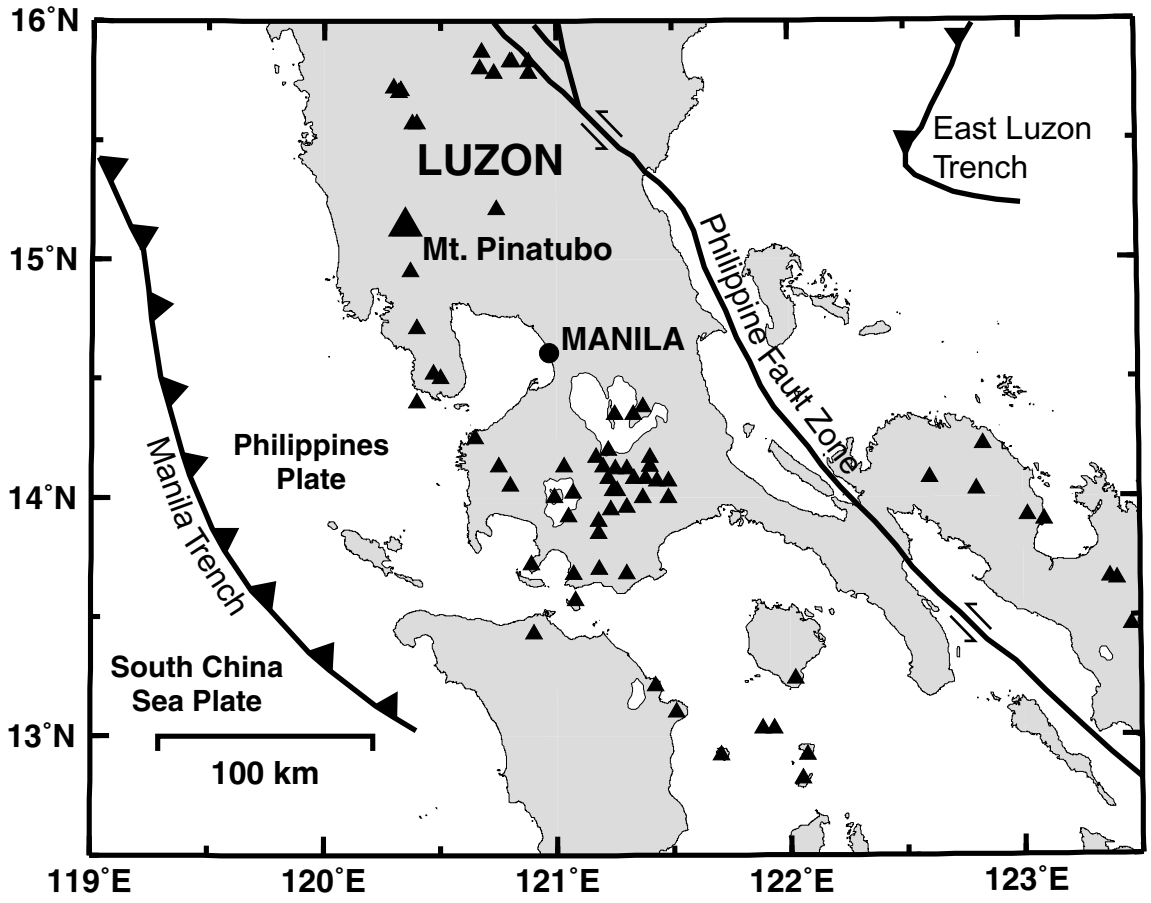

Figure 1. Location map of Mt. Pinatubo area. Shows locations of selected volcanoes (triangles) and regional tectonic features.

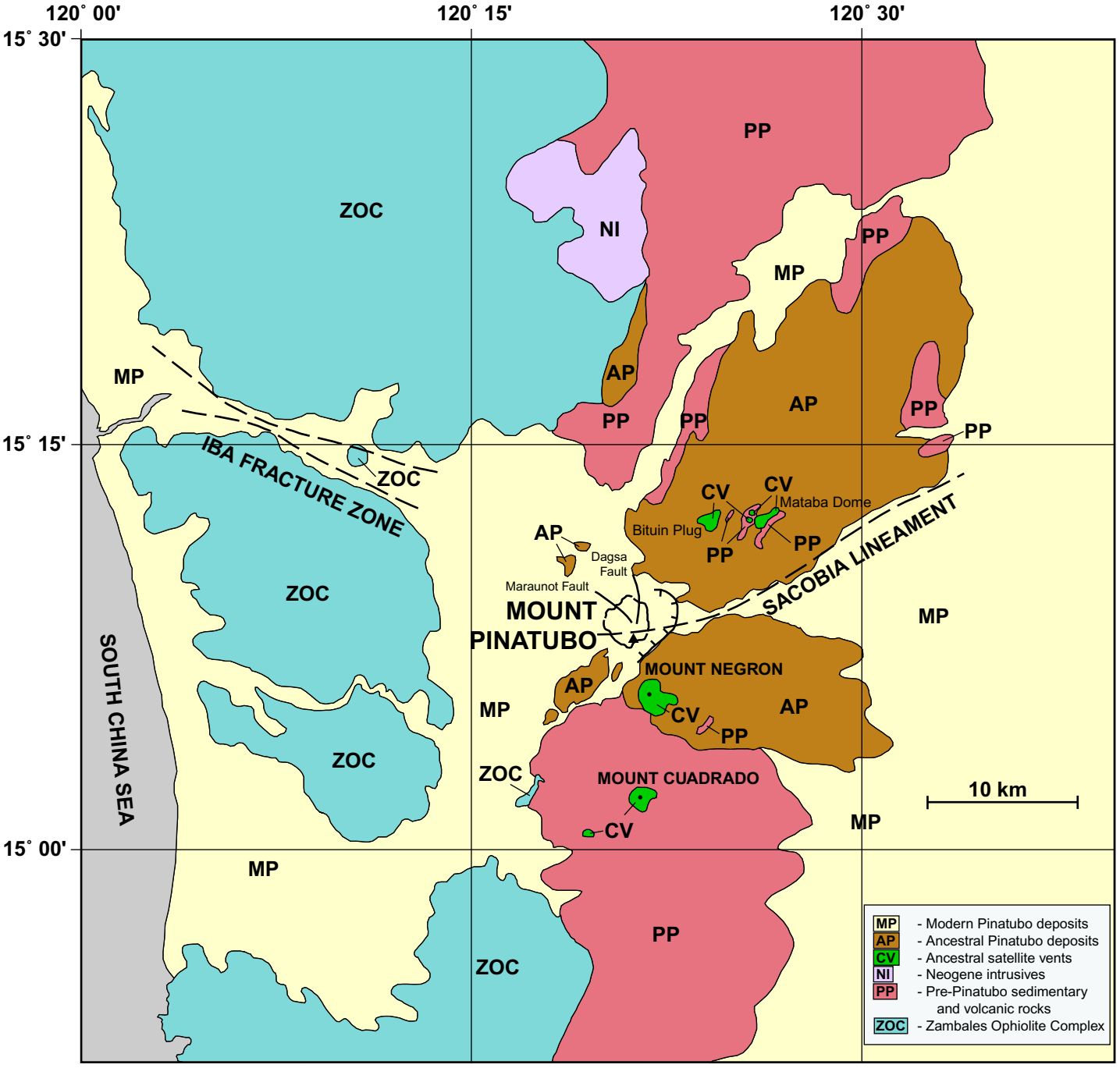

Figure 2. Generalized surface geology of the Mt. Pinatubo region. (Adapted from Newhall et al., 1996.)

Data and Initial Hypocenters

In April 1991, after roughly 500 years of relative quiet, Pinatubo showed signs of renewed volcanic activity. Because of the close proximity of U.S. Clark Air Base, the U.S. Air Force contacted the USGS and requested that a team be sent to monitor the activity of the volcano. The USGS, working with Filipino authorities, deployed a portable seismic network and recorded small earthquakes from early May until mid-June, when the volcano erupted and destroyed a majority of the stations. After the eruption, the network was rebuilt and monitoring continued until mid-August. The network consisted of instruments provided by the USGS Volcano Disaster Assistance Program (VDAP). These instruments were deployed at a total of twelve station locations. Seven of these locations were used for pre-eruption stations and only two survived the June 15 eruption. The other five stations were replaced on June 27 at different locations. Two of the twelve stations had three components (both pre-eruption - one survived) and one had a long-period component (post-eruption) [*Lockhart et al.*, 1996]. Ten of the twelve station locations were within a 40 km radius of the summit of Mt. Pinatubo, and two were considerably farther away (Figure 3). The station coverage was sparse, with spacing ranging from 10-20 km between nearest neighboring stations. The pre-eruption stations were clustered slightly tighter than the post-eruption stations, and the coverage was more evenly distributed around the summit. The post-eruption stations were focused around the area to the southeast of the summit, with no coverage northwest of the summit. Both station arrays favor the area to the east of the summit, with the pre-eruption stations covering an area slightly north of the post-eruption coverage area.

P-wave arrival times, from 3,007 earthquakes, picked for each pre-eruption station from May 6 until June 10, and for each post-eruption station from June 27 to August 21 were used in the present inversion. Picking was performed by the USGS and the method is currently unknown due to the lack of documentation. The recorded arrival times were edited visually at Virginia Tech for obvious errors, such as the P-wave being recorded before the S-wave for the same event. Repeated records of the same event were also removed. Only events with four or more arrivals were used. Initial hypocenters for the 3-D tomography were obtained using the program HYPOELLIPSE of *Lahr* [1989]. S-wave arrivals were used for the initial location of hypocenters, but are too sparse to be used in the velocity inversion. These hypocenters were located using three different 1-D velocity models. The velocities in these models increase linearly with depth. These same velocity models were used as starting models for the 3-D tomography. Only hypocenters that were located within the horizontal extent of the 12 station array (azimuthal gap less than 180 degrees) were used in the inversion.

A statistical estimate of the constraint of focal depths was obtained for both the pre- and post-eruption networks. The following analysis was conducted for earthquakes at three different depths in the center of the model. A sample event was placed at depth, and travel times to each of the stations were calculated (with random noise on the order of the estimated picking error added to the times) using a linearly increasing velocity model. Keeping the depth fixed, the event was then located horizontally using the program HYPOELLIPSE, and an RMS travel time residual was calculated for the event. The fixed depth was varied over several kilometers both above and below the actual depth and a residual was calculated for each fixed depth. The plots of the calculated residuals for each location are shown in Figure 4. From these results, it appears that the pre-eruption station array provides a better depth constraint than the post-eruption array for hypocenters within the upper 12 km of the model (shallow events). Although neither array handles deeper events very well, the post-eruption array appears to be somewhat better at

constraining depths than the pre-eruption array. These results assume that the velocity structure is known, and the events were placed near the center of the model; therefore they provide an estimate of the best possible constraint for the earthquakes in this study.

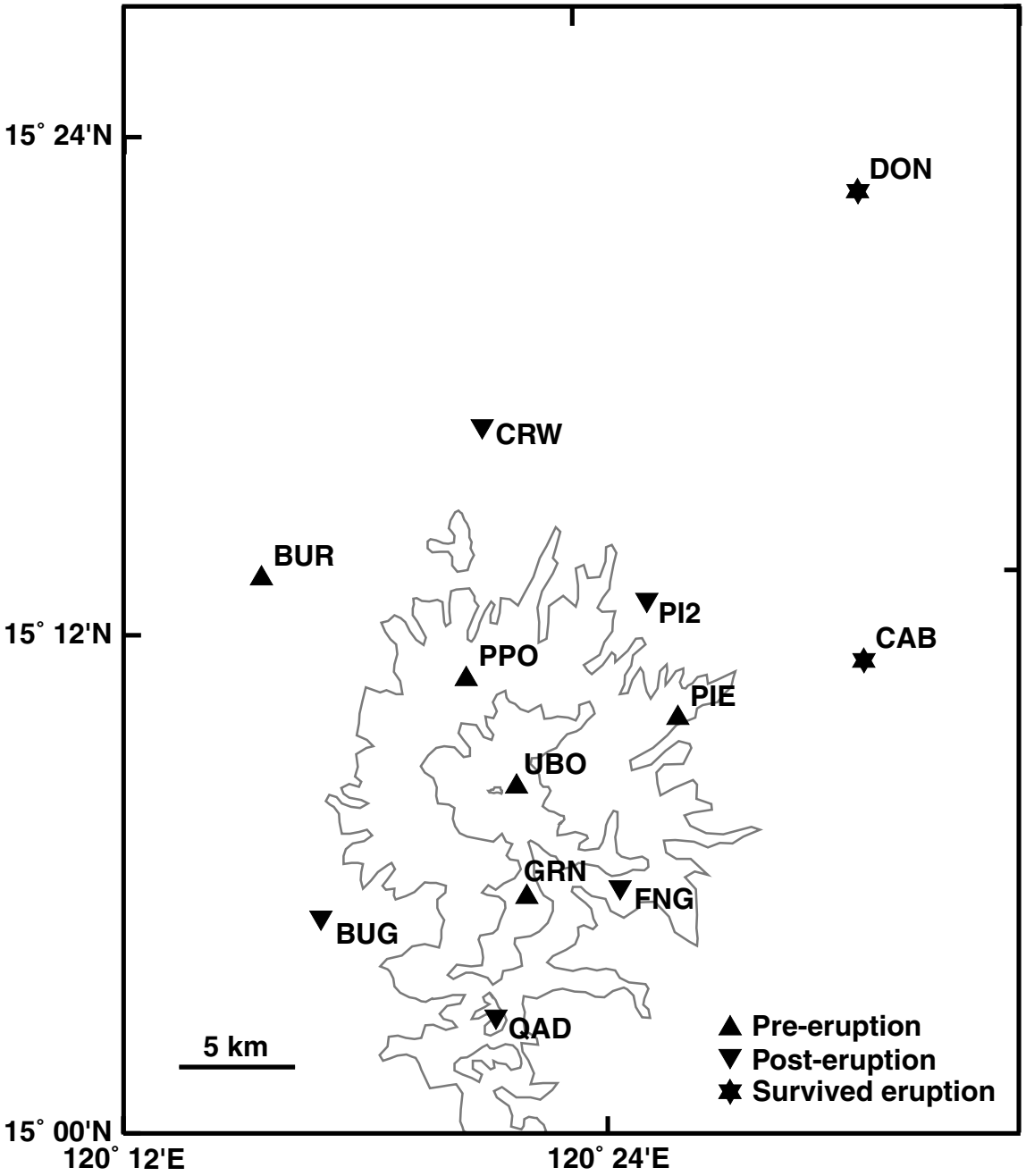

Figure 3. Locations of all pre- and post-eruption recording stations used in inversion. Area of figure equivalent to study area. Pinatubo summit topography shown. Contour interval 500 meters, summit is 1745 meters (pre-eruption). Three letter symbols indicate station identifiers.

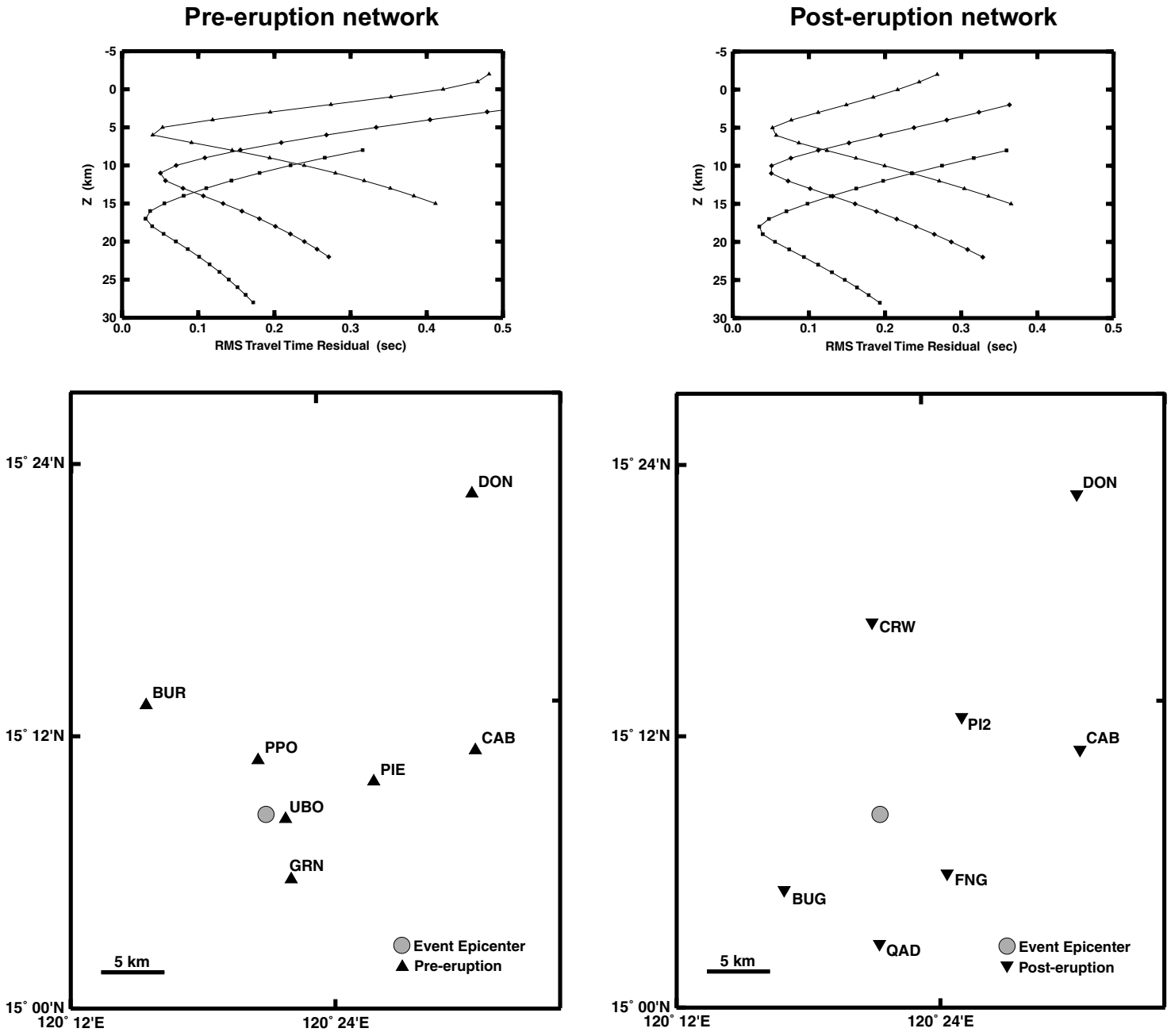

Figure 4. RMS travel time residuals for synthetic hypocenters at trial depths within the initial model. Maps show respective station networks and event epicenters. See text for explanation.

Inversion Algorithm

Earthquake arrival times were inverted the for three-dimensional velocity structure beneath Mt. Pinatubo using the tomography algorithm of *Hole et al.,* [2000]. Travel times and ray paths are calculated using a finite difference solution to the eikonal equation initially developed by *Vidale* [1990]. There are two well-documented limitations to this algorithm: it cannot handle sharp velocity contrasts and it calculates only first arrival travel times. The first limitation was corrected by *Hole and Zelt* [1995]. The second limitation is inconsequential if the first arrival is large enough to be picked from the records. When the first arrival is similar in amplitude to the station noise level and subsequent phases are larger, then the wrong phase is picked and error is introduced.

The inversion method used here separates the joint inversion of velocities and hypocenters, holding one fixed while the other is adjusted. The researcher has the option of controlling the number and sequence of velocity and hypocenter inversions. By interweaving velocity adjustments and hypocenter relocations, the user is able to control and explore the nonlinear tradeoff between velocity, hypocenter spatial location and origin time. Ray paths are dependent upon the slowness model, and only small perturbations of this model are allowed without significantly changing the ray paths. Therefore, a slow convergence toward a stable solution is desired. If convergence is sufficiently slow, this scheme of iteratively solving the linearized velocity and linearized hypocenter inversions is an effective approximation of simultaneous linearized inversion, which in turn is an approximation of the coupled nonlinear problem [*Hole et al.*, 2000]. An appropriate choice of velocity model smoothing size and convergence rate (decrease in smoothing size) also allows the inversion to properly model large-scale velocity structure with early iterations, while later iterations model increasingly complex structures.

The principle of reciprocity states that travel times and ray paths are equal between two points, regardless of the direction of propagation. Therefore, because the number of stations is significantly lower than the number of hypocenters, the travel times and ray paths are calculated using the stations as sources and the hypocenters as receivers. This amounts to a significant savings in computation time, because the finite difference eikonal equation algorithm calculates travel times to every grid node within the model. Stations and earthquakes are not required to be located directly at grid nodes. To complete the total travel time from source to receiver, the time within the cell is found by tri-linear interpolation. This is the linear interpolation in each direction, but averaged over the 8 grid points surrounding the cell. This is deemed to be a sufficient approximation because it is consistent with the finite difference approximation. Rays are then traced from each hypocenter back to the station. These rays are geometrically perpendicular to the wave fronts and mathematically parallel to the local travel time gradient. The travel time misfit is applied equally along the ray path and an equal slowness perturbation is added to each of the cells intersected by the ray. This is a form of backprojection tomography. These perturbations, along with a count of ray intersections for each cell, are summed for all ray paths from that source. This process is repeated for each source, with a record of the summed perturbations and ray intersections for each cell being acquired for the total set of source-receiver pairs. Ideally, this summation of perturbations will lead to cancellation of perturbations (destructive interference) for cells which already have accurate velocity values and to the appropriate correction (constructive interference) for those cells in which a velocity anomaly exists. This means that high ray sampling in all cells is desired in order to accurately model the velocity structure.

Due to the irregularity of ray coverage within the model volume, if the model is densely gridded, many grid cells are poorly sampled or are not sampled by rays. Therefore, the slowness perturbation model produced by the above procedure typically contains many cells which have little or no perturbation applied to them. This is a rough model, which means that there are cells which have had a significant slowness adjustment adjacent to cells which have had little or no adjustment. Another problem with this poorly sampled model is that the velocity values in cells which have little or no cumulative ray coverage do not get adjusted to a more realistic value even though neighboring cells are receiving significant adjustments. This leaves many cells with highly inappropriate velocity values which are often virtually the same as the starting velocity values.

To counteract these effects, a smoothing scheme is adopted which averages values from neighboring cells to ensure a smooth gradient across the model with no artifacts of poor ray coverage. First, a weighted average slowness perturbation model is produced by averaging the effect of each of the perturbations caused by intersecting rays (within the specified volume) in such a way that perturbations caused by rays close to the central grid node are given a higher weighting than those farther away. The weighted average slowness perturbation model is produced by taking the summed slowness perturbations from a specified number of cells around each grid node and dividing by the count of ray intersections for the total averaging volume. In practice, this only approximates the closest ray weighted average, as cells that have a higher number of intersecting rays get a higher weighting, regardless of the closeness to the grid node (as long as they are within the averaging volume). After the "ray smoothing" is applied, creating a weighted average slowness perturbation model, a 3-dimensional moving average filter is applied across the entire model volume. The number of cells chosen for the above smoothing size, along with the grid spacing, determines the volume of the slowness perturbation model that is averaged to produce the new velocity value at each node in the new model. This densely gridded, smoothed model approach is preferred over the coarsely gridded model because it allows for the resolution of smaller objects and optimum fidelity. The concept of good fidelity implies that objects are at their correct locations and shapes rather than being forced to take the locations and shapes of the model blocks. The parameterization should be chosen to allow the resolution of the smallest objects that can be detected by the data [*Hole et al.*, 2000].

The effect of ignoring the intrinsic coupling between earthquake hypocenters and velocity structure is well documented. *Thurber* [1992] shows that this will generally produce a biased velocity model containing artifacts and having anomalies that are significantly underestimated. The typical solution to this issue is to invert simultaneously for both velocity structure and hypocenters, while optimizing the trade-off between them. Since this trade-off is unknown, the method of allowing only one parameter at a time to be adjusted is preferred here. This allows for the relationship between hypocenters and velocity structure to be explored and reduces the number of artifacts due to inaccurate hypocenters.

The tomography algorithm described above was initially developed for use with controlled-source seismic surveys, but was extended to allow the relocation of earthquake hypocenters [*Hole et al.*, 2000]. The inversion for hypocenter parameters (X, Y Z, and T) is linearized assuming that a small perturbation of the earthquake location will produce a small perturbation of the observed travel times. Travel times for each source-receiver pair are calculated in the same manner as described above. Partial derivatives with respect to the x-, y-, and z-directions, as well as the travel time residual, for each travel time are calculated at the unperturbed hypocenter. The partial derivatives are obtained as finite differences by calculating

the average travel time gradient across the grid cell containing the hypocenter, and the travel time within the grid cell is found by trilinear interpolation [*Hole et al.*, 2000]. The gradients and residuals are recorded for each source-receiver pair and are sorted by earthquake. The set of linearized equations for each earthquake is inverted using singular value decomposition (SVD). If an earthquake was recorded on fewer than four stations, or if a hypocenter is poorly constrained (indicated by singular values that are four orders of magnitude smaller than the maximum) then the earthquake is discarded from the inversion. The finite-difference travel time algorithm allows stations to be placed anywhere in the model; therefore, station-elevation corrections are not needed to remove the effect of near-station geology. Instead, near station geology is included in the densely gridded velocity tomography.

Analysis

Velocity Models

All of the velocity models cover the same volume of 40 x 50 x 34 km (Figure 3), which was chosen to include all seismic stations within the network referred to above. The models are composed of cubic blocks with 1 sq. km sides. Three kilometer "buffer zones" of low velocity at the top and bottom of the model help to ensure containment of rays within the model. The top of the model is 5 km above sea level (2 km volcano summit plus 3 km buffer) and the base is 28 km below sea level.

Several inversions were performed with different starting models and inversion parameters. All of the initial 1-D models consisted of a linear velocity increase with depth. The initial hypocenter locations were produced by HYPOELLIPSE within these simple velocity models, as discussed previously. Variations in the starting velocity model included different vertical gradients and velocity ranges. The initial horizontal smoothing size of 20 x 20 km was chosen based on the size of the expected area of good ray coverage, which is roughly equal to the area of good station coverage. The smoothing size was reduced by two-thirds after three velocity iterations and one hypocenter iteration. This rate was chosen to allow the algorithm sufficient time to model large scale velocities without "wasting" iterations. The ratio of horizontal to vertical smoothing dimension was chosen to be 2:1. The relatively slow convergence scheme is preferred to reduce dependence of the final model on the starting model [*Hole et al.*, 2000]. This convergence scheme was chosen based on the results of testing by *Hole et al.* [2000] which show that this ratio of velocity adjustments to hypocenter relocations is sufficient to allow the hypocenters to adequately track the changes in the velocity model. Preliminary testing showed this to be the case with the current data as well (Table 1 and Figure 5). Table 1 shows the significant difference between travel time misfits from the preferred scheme and the results obtained using fixed hypocenters. This reinforces the idea that allowing hypocenters to be relocated within the updated models is essential if tomography is to produce reliable results. Figure 5 shows that the first hypocenter relocation moves the hypocenters approximately 90 percent of their total relocation distance. Table 2 shows that early hypocenter relocations produced larger reductions in travel time residuals, suggesting that perhaps a scheme allowing early floating hypocenters might have improved the effectiveness of early velocity adjustments. Later hypocenter relocations produced small reductions in residuals similar to those produced by late velocity iterations.

Several starting velocity models were tested using the same convergence scheme (Figure 6). All initial, one-dimensional models contain simple linear velocity increases in an effort to reduce the amount of structure imposed on the final model by the starting model. The preferred model used a linear velocity increase that roughly approximates the vertical velocity profile produced by the preliminary work of the 1991 Pinatubo eruption investigators (Figure 6). Their preliminary model is more complex than a simple linear velocity increase (velocities in their model increase rapidly at near surface depths and very slowly at depths over 10 km). Therefore, the preferred model cannot match their preliminary model at all depths. The preferred model was designed to balance the mismatch at all depths, and contains lower velocities (than their preliminary model) at the near surface and higher velocities at greater depths. Two other models were chosen to be end members around this moderate model, one model being a steep linear velocity increase and the other a shallow linear increase. Figure 6 shows the average velocity profiles of the initial and final models for the steep gradient, shallow gradient, and preferred

models. Another velocity model was tested which matched the shallow velocities of the preliminary model and contains higher velocities at depth.

Inversions with all of the different initial models produced similar lateral velocity variations within the well-constrained volume of the model. The large range of absolute velocities obtained indicates that the absolute velocities are not well-constrained and is probably due to the heavy trade-off between hypocenter depths (and origin times) and the vertical velocity profile. The preferred model appears to be the most stable and has the least amount of extreme velocity variations, especially at the edges of the ray coverage volume. There are three distinct zones of relative low velocity (termed LVZ1-3) present in the final preferred model, which are discussed in greater detail below. Horizontal slices at selected depths through the preferred model are shown in Figure 7.

Hypocenters

The final hypocenters in this study contain the same large scale features seen by previous researchers and are described above. The relative trends differ only in detail. There are groups of pre-eruption hypocenters tracing out apparently curved surfaces, and some potentially planar groups found within the post-eruption hypocenters. These features are further discussed below. The RMS travel time residual after hypocenter relocation within the final velocity model was reduced by 51% from an initial value of 180 ms (Table 2). The average relocation distance after the final hypocenter inversion is 2.55 km, with an average horizontal relocation of about 1 km and a vertical relocation of about 2.2 km. The final hypocenters are an average of about 1.9 km deeper than the initial hypocenters located within the preferred 1-D linear gradient starting model.

Table 1. Travel time misfits for selected models.

Model name	Convergence scheme (iterations at each smoothing size)	Final RMS travel time misfit (ms) within 4x4x2 km smoothed model
Final (Preferred)	vel, vel, vel, hypo	84
Steep Velocity Gradient	vel, vel, vel, hypo	83
Shallow Velocity Gradient	vel, vel, vel, hypo	83
Fixed Hypocenters	vel	151
Floating Hypocenters	vel, hypo	88

Table 2. Travel time misfits after each iteration of final (preferred) model.

Iteration #	Smoothing size (km)	Iteration type	RMS travel time misfit (ms)
0	Initial Model	NA	180
1	20 x 20 x 10	linearized velocity	173
2	20 x 20 x 10	linearized velocity	170
3	20 x 20 x 10	linearized velocity	169
4	20 x 20 x 10	linearized hypocenter	122
5	12 x 12 x 6	linearized velocity	118
6	12 x 12 x 6	linearized velocity	117
7	12 x 12 x 6	linearized velocity	117
8	12 x 12 x 6	linearized hypocenter	91
9	8 x 8 x 4	linearized velocity	90
10	8 x 8 x 4	linearized velocity	89
11	8 x 8 x 4	linearized velocity	88
12	8 x 8 x 4	linearized hypocenter	88
13	4 x 4 x 2	linearized velocity	86
14	4 x 4 x 2	linearized velocity	85
15	4 x 4 x 2	linearized velocity	84
16	4 x 4 x 2	linearized hypocenter	84

Resolution of Velocity Models

There are two distinct ideas of how to estimate the resolution of models produced by tomography. For algorithms that directly invert the data kernel matrix, some variation of the resolution matrix, derived from the set of model parameters, is employed to estimate how well the model is parameterized. This value is termed the model parameter resolution, and estimates whether the choice of grid density is optimized to fit the data geometry and chosen algorithm. While this method provides some useful information, the problem with the approach is that the values it returns can be improved by using fewer grid nodes and effectively under-parameterizing the model to fit poor data coverage. This results in each of the model cells being well-resolved, but if the number of model blocks is insufficient to model the volume properly, the subsurface is not well-resolved in space. Under-parameterizing also has the effect of increasing the data misfit (travel time residuals), because the under-parameterized model does not contain the complexity needed to fit the data adequately. The idea of spatial resolution is a more accurate estimation of the size of the smallest object that can be seen with the given experiment. Any approach yielding spatial resolution is inherently design driven rather than model driven, and is here preferred because of that distinction. While the resolution matrix approach described above can be used to obtain an estimate of spatial resolution, checkerboard testing is commonly performed and is described in further detail below.

Apart from the accuracy of arrival time data, spatial resolution within the velocity model is dependent upon the density and orientation of ray coverage within the model blocks, which is dependent upon the number of stations and hypocenters and their relative locations. Two independent techniques were employed to quantify the spatial resolution within the velocity model. Visual observation of ray streaking within the velocity model is an indication that the solution has been over-modeled. Ray streaking is the appearance of velocity anomalies with shapes that are oriented parallel to the dominant direction of local rays. Over-modeling manifests itself as artifacts that are a result of non-uniqueness features due to incomplete ray coverage within the model. The smoothing size at which these over-modeling effects were observed is an estimate of spatial resolution. Spatial resolution is also estimated by synthetic re-creation of checkerboard velocity models. This is accomplished by performing tomography with the given set of hypocenters and station coverage, using synthetic travel times calculated in a checkerboard velocity model. The checkerboard model is created by superimposing a checkerboard pattern onto a generic starting model. Small random errors are added to the times to simulate picking error and noise. These synthetic travel times, along with initial hypocenters and the preferred starting velocity model, are used to invert for the checkerboard pattern using a convergence scheme common to the inversion.

Horizontal checkerboard sizes of 15, 12, 10, 8, 6, 5, 4 and 2 km were superimposed on a vertical, linear velocity increase. These sizes were tested to estimate the smallest size that could be constrained by the tomography algorithm (Figures 9-10, and Appendix). For each checkerboard size, several inversions were performed. The locations of the velocity anomalies were shifted from their original configuration by one-half wavelength in both horizontal directions for the second configuration and by one complete wavelength in one horizontal direction for the third configuration, with all other parameters remaining the same. Since the true locations of the hypocenters are known, the ability of the tomography algorithm to move the hypocenters to their proper locations within the checkerboard models was also tested (Table 3). For checkerboard sizes larger than 6 km, synthetic travel times were calculated from both the initial hypocenters (configuration 4) and the preferred final hypocenters. The inversions which

used the final preferred hypocenters were less stable, especially at depth, than the inversions that started with the correct (initial) hypocenters. Due to the already decreased stability of the smaller checkerboard models, the smaller sizes were not tested in this manner.

Checkerboard sizes from 15 km down to 4 km were successfully reproduced by the tomography algorithm within certain portions of the model. (Figures 9-10, and Appendix show the results of the synthetic recreations, from larger to smaller checkerboard sizes.) The volume of the model in which the 4 km checkerboards are reproduced is relatively small; therefore, a significant amount of smearing exists around the zone of good recovery. The volume in which good recovery of any particular checkerboard size exists is slightly smaller than the total size of four neighboring anomalies. This results in only the center portion of a group of four anomalies being properly recreated and the outside portion being smeared or truncated. Amplitudes of anomalies were recovered by about a maximum of 75% for the larger checkerboard sizes, with lows generally being better recovered than highs. For the smaller checkerboard sizes, typical recovery was about 40-50%, but that number decreased with decreasing checkerboard size. In order to ensure stability of the inversion, the amplitudes of the anomalies were reduced for each smaller checkerboard size so that a similar velocity gradient existed in each model.

Table 3. Hypocenter location misfits for selected synthetic inversions.

Checkerboard Size (km)	Hypocenter Iterations	Hypocenter Location Misfit (km)
5	**1**	1.23
5	**2**	1.14
5	**3**	1.09
5	**4**	1.04
5	**5**	1.01
15	**4**	0.81
12	**4**	0.94
10	**4**	1.18
8	**4**	1.25
6	**4**	1.31
4	**4**	2.32
2	**4**	1.22

Discussion of Resolution

The inability of the tomography algorithm to converge to similar average velocity profiles given a variety of starting models is somewhat discouraging and demonstrates that the results are heavily dependent upon the starting model. This dependence was reduced by using the slow convergence scheme discussed above. An optimal 1-D starting model is almost definitely more complex than the simple linear gradient models used here. Without any observation-based reason to choose any one particular complex 1-D model, the temptation to use such a model was resisted. The lack of accurate absolute velocities, as indicated by the non-unique solution, does not necessarily require the inaccuracy of the relative velocity variations observed within the well-resolved portions of the model. Several initial models were tested and the anomalous features discussed above appeared in similar locations and strengths in all of the models. This indicates that the relative velocities in horizontal slices are being accurately modeled despite the inability of the algorithm to arrive at absolute velocities independent of initial velocities.

The resolving power of the ray coverage model was thoroughly examined using synthetic checkerboard recreation tests. These tests are generally regarded as a good measure of the spatial resolution within the model, but are not without shortcomings. The synthetic travel times are calculated within the checkerboard model from every hypocenter to the stations that actually recorded the corresponding real event. This makes every ray path within the synthetic model accurate and does not account for the existence of bad data. These bad data without question exist within the real data; therefore, the resolutions obtained are best-possible estimates. If the amount of bad data is significant, the actual resolution is greatly diminished. Another problem with the synthetic tests is their inability to handle inaccurate initial hypocenters. The synthetic travel times were calculated using the final preferred hypocenters. For some checkerboard re-creations, the initial hypocenters used in the real inversions were used as initial hypocenters for the synthetic inversion. These tests that required the algorithm to relocate hypocenters over significant distances were unstable, especially at depth. Figures 9 and 10 show one example of the difference in results obtained from using accurate versus inaccurate initial hypocenters. This instability is probably the result of the difference between the complex ray paths traced through the checkerboard model and the simple ray paths traced through the 1-D initial model. This instability increased as the checkerboard size decreased, which further magnified the difference between complex synthetic rays and simple initial rays. The tests using initial hypocenters different from the hypocenters used to calculate synthetic travel times were abandoned for small checkerboard sizes. This is probably not important, because the actual velocity structure beneath Pinatubo is likely less complex than the small checkerboard models.

Perhaps the largest trade-off in the tomographic solution is between the hypocenter depths, their origin times and the 1-D velocity profile. This trade-off is not resolvable without some additional constraint being placed on the parameters. The problem is particularly difficult in situations like Pinatubo, because of the small areal extent of the recording network and the resulting mostly near-vertical ray paths emanating from the hypocenters. In this situation, a shift in focal depth can be accomplished by adjusting the origin time or adjusting average 1-D velocities along the ray paths. Unless each hypocenter is recorded on several stations over a large area (allowing ray paths with significantly different takeoff angles) and either reliable average velocities or focal depths are available, no one solution is preferred over another. The consequences of this are seen in the cross-sections of the pre- and post-eruption seismicity shown in Figure 8. The average focal depth of hypocenters within the preferred model is greater than

that obtained by *Mori et al.*, [1996] and the concentration of near surface events is quite low. This is almost definitely not accurate and is most likely caused by near surface velocities being too slow. However, as discussed previously, without reliable a priori knowledge of velocities, a minimum structure initial model was preferred and the accuracy of absolute velocities was sacrificed. The shift in focal depths from their probable true locations is not believed to be large enough to cause significant variability in the velocity model and the occurrence of similar anomalies in models obtained with different initial velocities supports this conclusion.

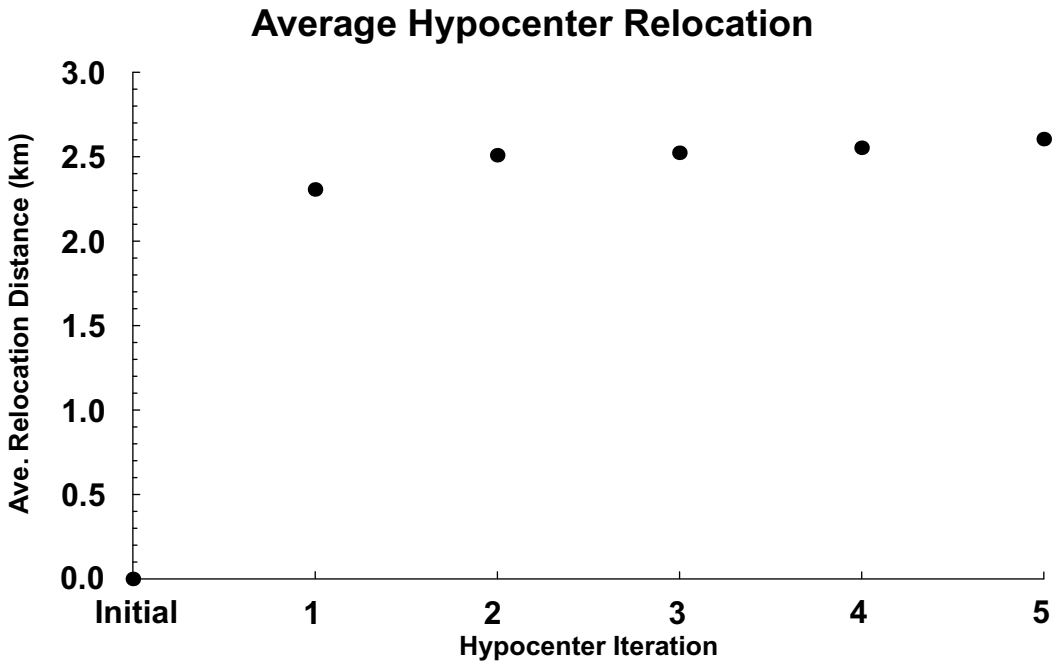

Figure 5. Average relocation distance from initial locations after each hypocenter inversion. Each hypocenter relocation occurs after three velocity structure adjustments. Note that 90% of relocation occurs in first iteration.

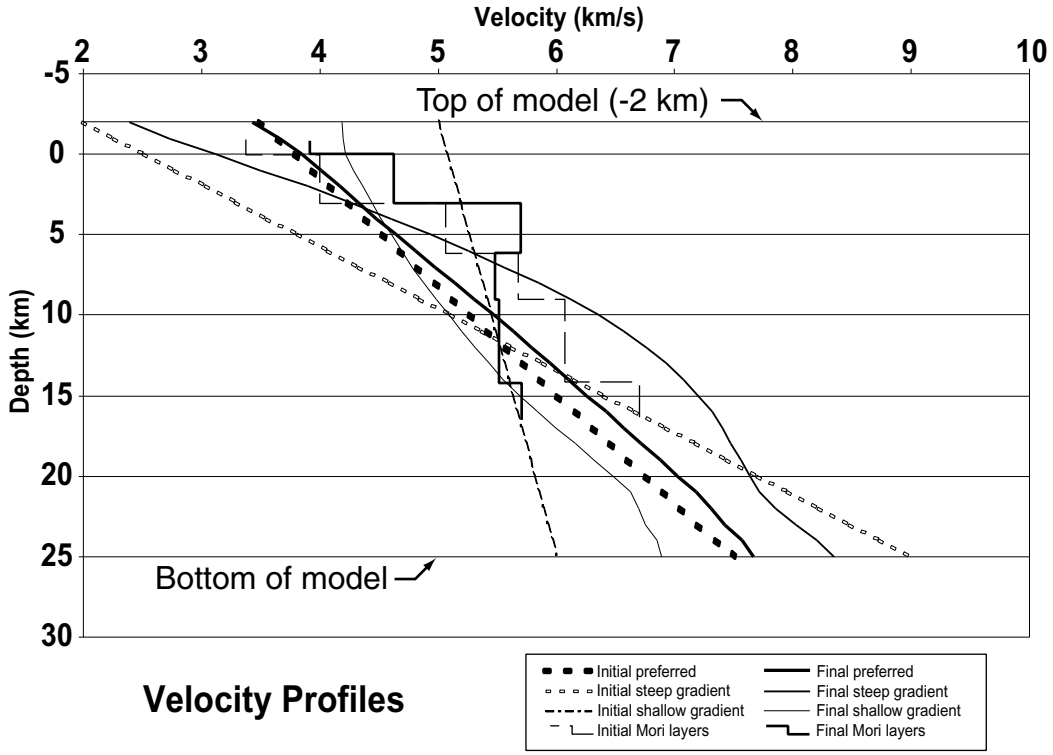

Figure 6. 1-D velocity profiles for selected models. Dashed lines represent initial models. Solid lines represent horizontally averaged final models.

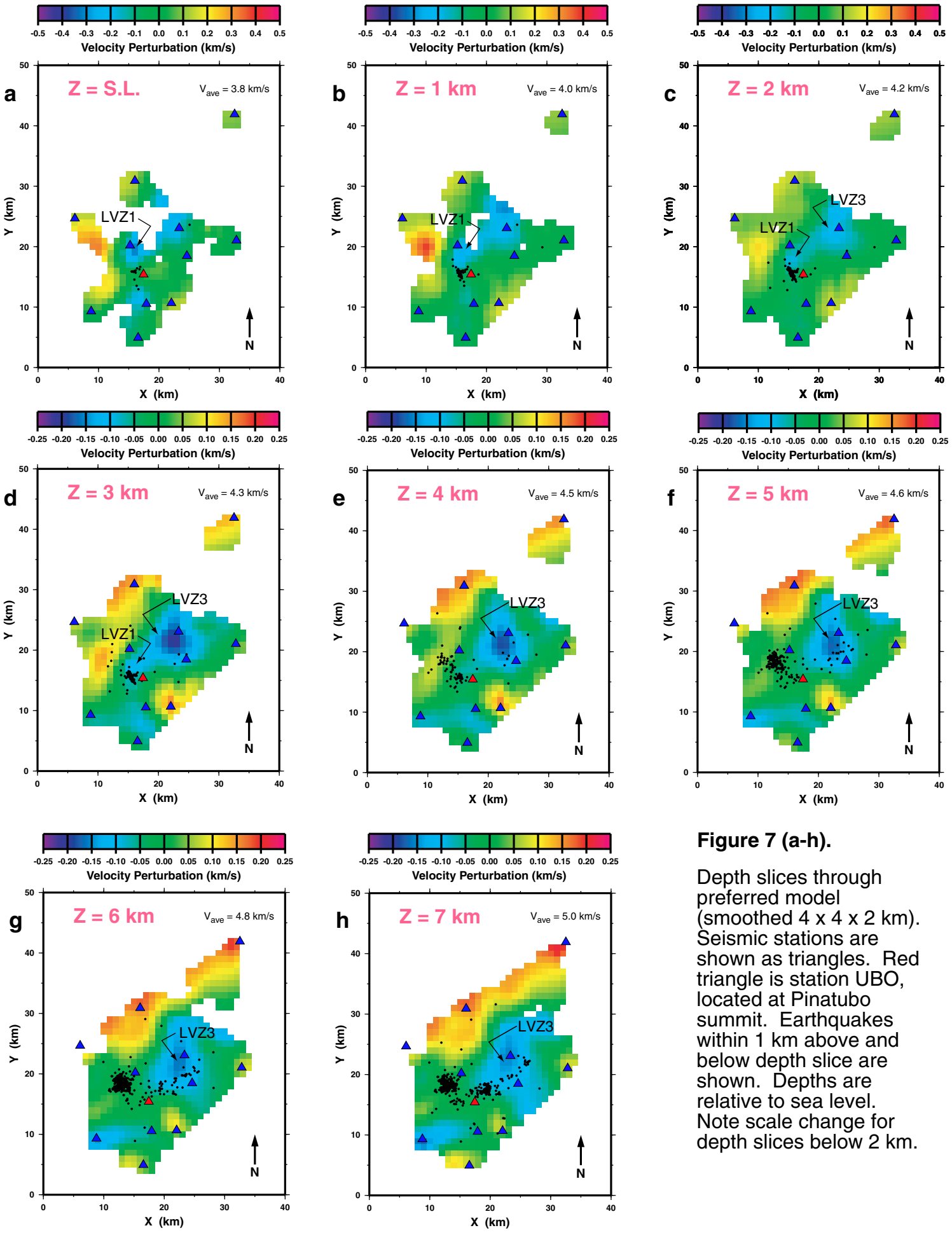

Figure 7 (a-h).

Depth slices through preferred model (smoothed 4 x 4 x 2 km). Seismic stations are shown as triangles. Red triangle is station UBO, located at Pinatubo summit. Earthquakes within 1 km above and below depth slice are shown. Depths are relative to sea level. Note scale change for depth slices below 2 km.

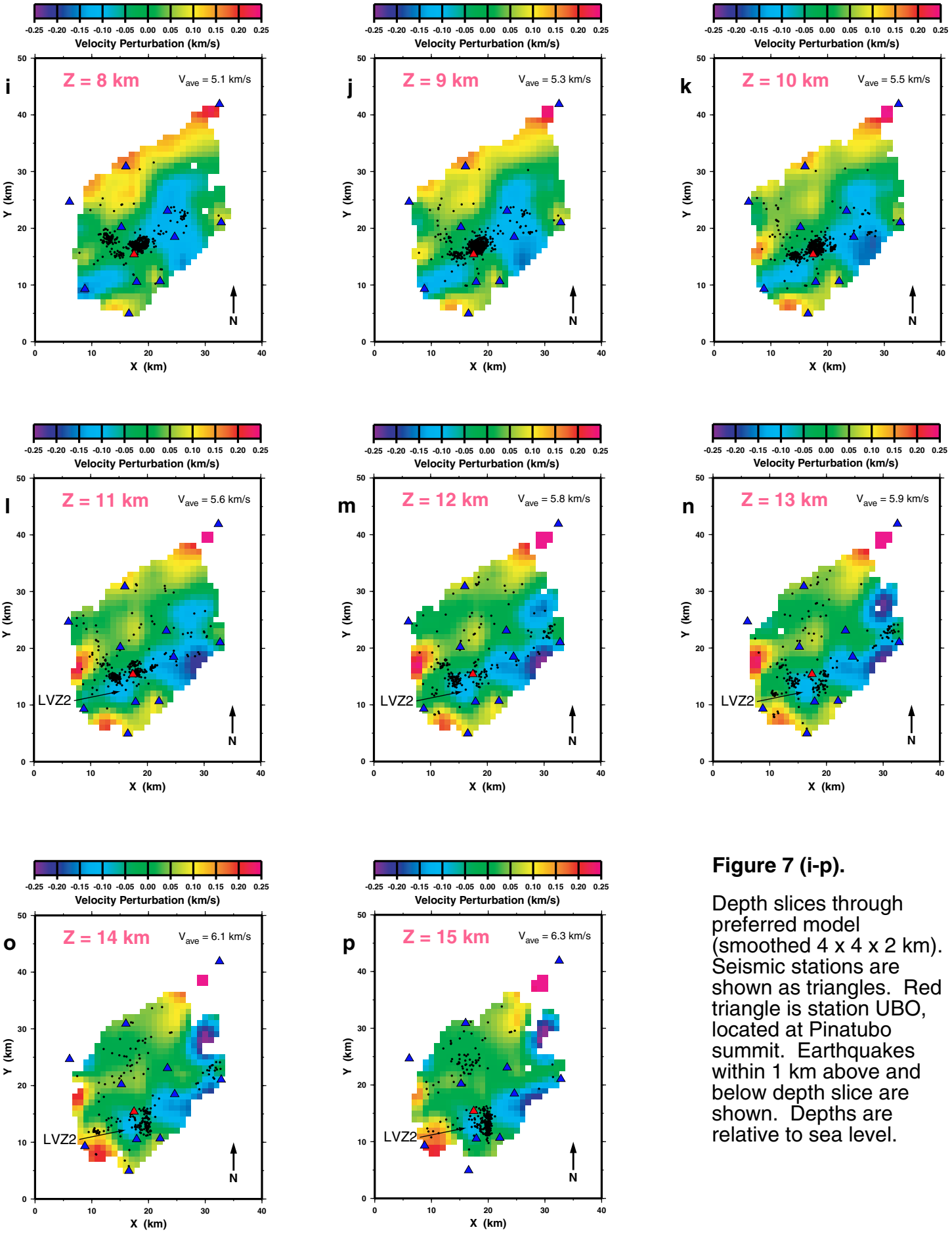

Figure 7 (i-p).

Depth slices through preferred model (smoothed 4 x 4 x 2 km). Seismic stations are shown as triangles. Red triangle is station UBO, located at Pinatubo summit. Earthquakes within 1 km above and below depth slice are shown. Depths are relative to sea level.

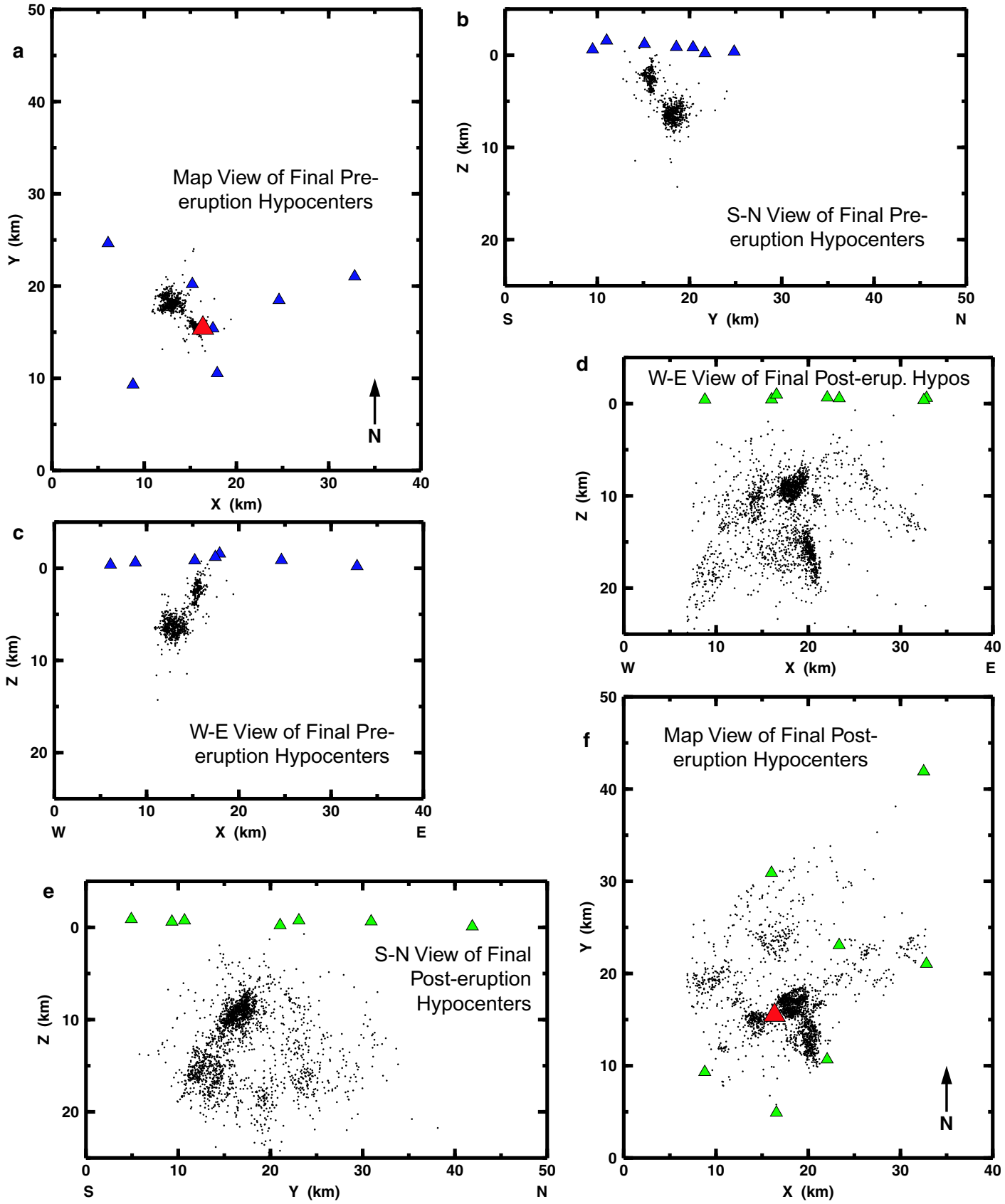

Figure 8. Final hypocenters after relocation within 4 x 4 x 2 km smoothed velocity model. Seismic stations are shown as triangles. (a-c) Pre-eruption plots. (d-f) Post-eruption plots. Depths are relative to sea level. Red triangle is Pinatubo summit.

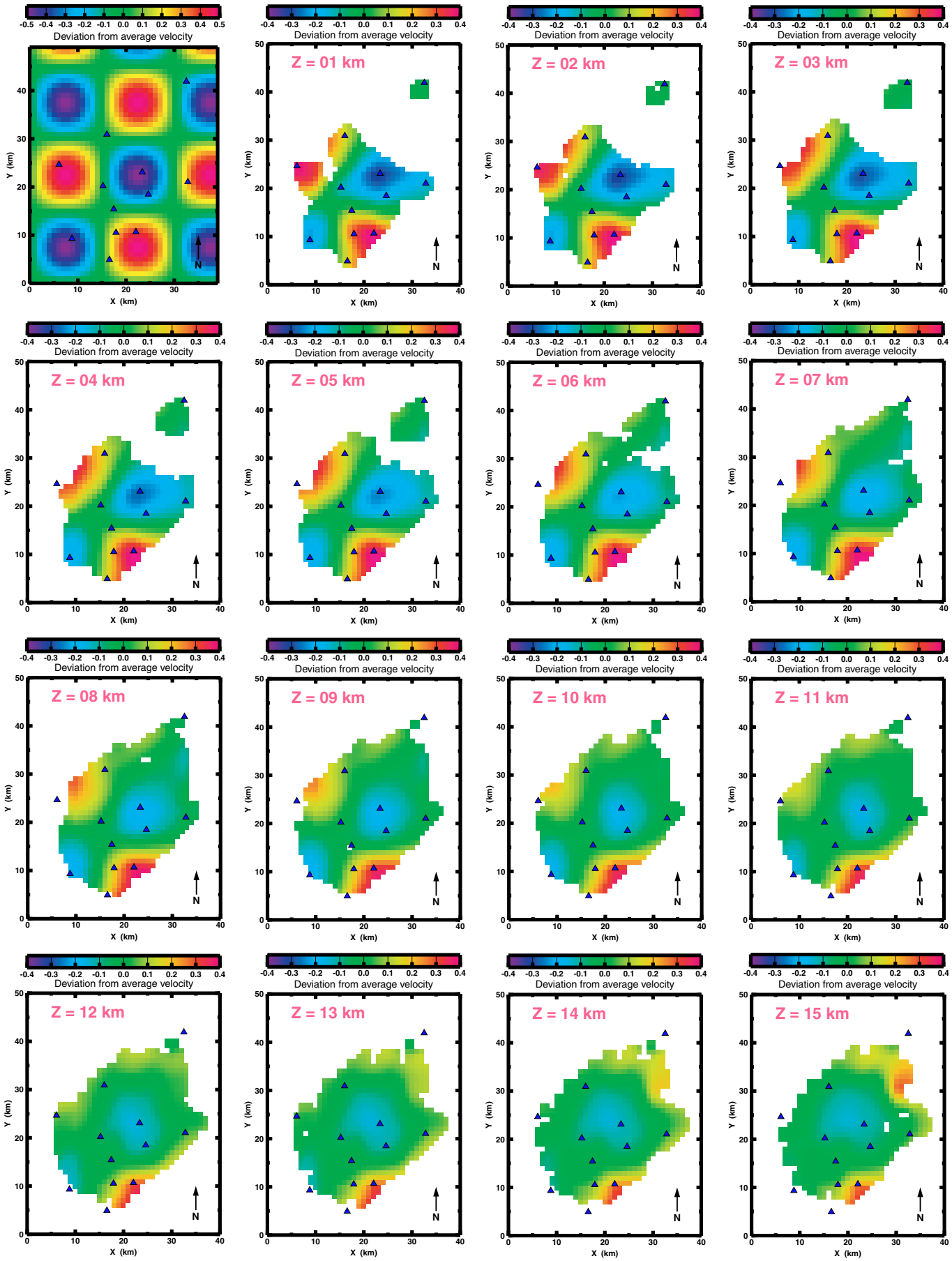

Figure 9. Depth slices through reconstructed 15 km checkerboard model (pattern configuration 4).

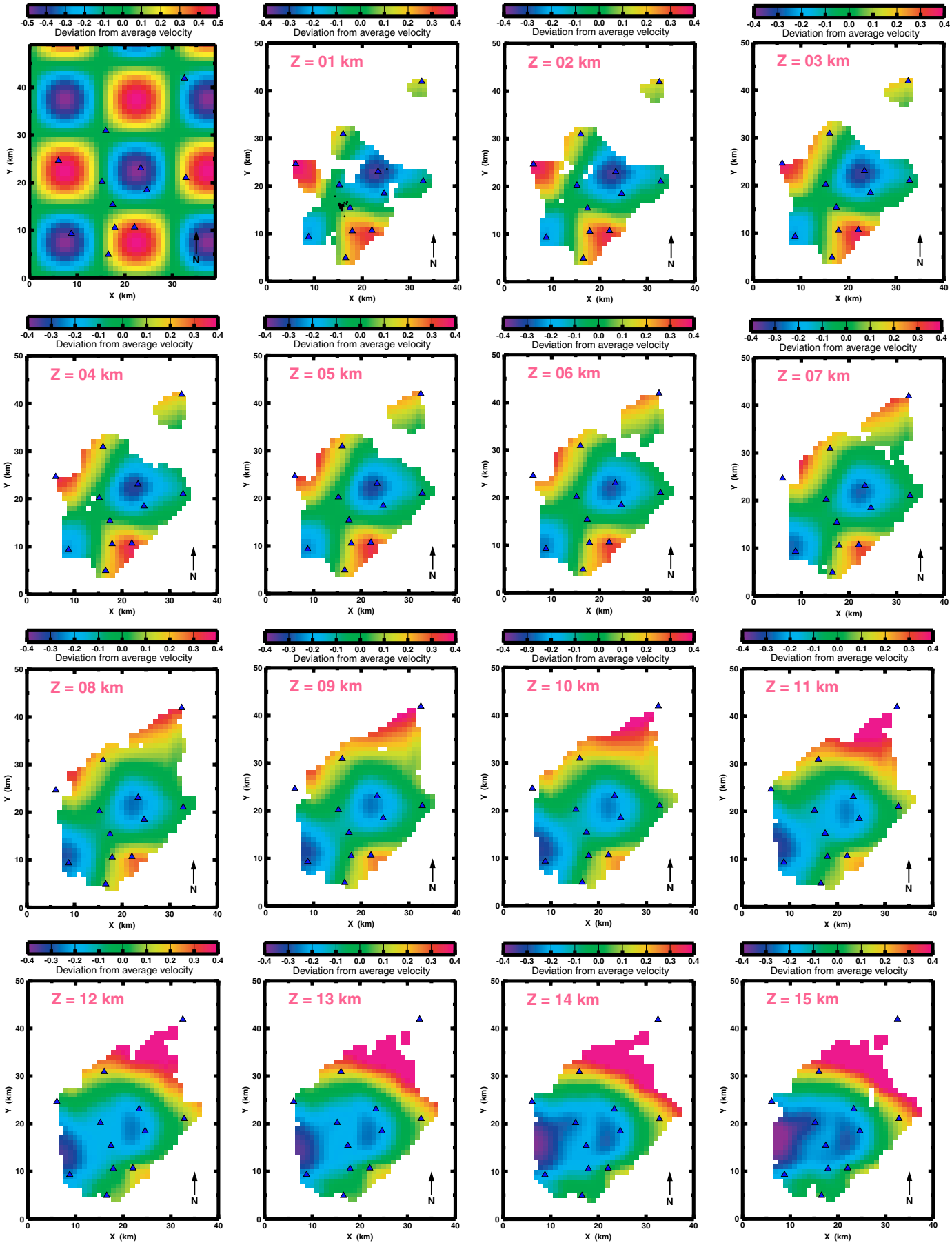

Figure 10. Depth slices through reconstructed 15 km checkerboard model (pattern configuration 3).

Interpretation

The non-unique nature of earthquake tomography makes interpretation of the results difficult. An infinite number of solutions that adequately fit the arrival time data are possible due to the combination of the large number of unknowns, the presence of bad and noisy data, and the lack of adequate ray sampling within the model. The non-unique solution is examined by varying starting parameters and convergence schemes to test the robustness of the final model and its dependence upon the several algorithm parameters. This gives some insight into the validity of features found in the final model.

Velocity Model

Three distinct zones of relative low velocity (with respect to the average velocity at a particular depth) are present within well-resolved portions of the model. A shallow low velocity body (LVZ1, Figure 7 a-d) 2-4 km wide is centered approximately 3 km northwest of the Pinatubo summit and extends from near the surface to about 3 km below sea level (≈5 km below the Pinatubo summit). This is in agreement with the "northwest" or "summit" LVZ previously identified by *Mori et al.* [1996]. A deep low velocity body (LVZ2 Figure 7 l-p) 3-5 km wide is centered 3-4 km southwest of the summit and extends from ≈10 km b.s.l. to over 15 km b.s.l. The top and bottom of this LVZ are not well constrained because of ray streaking (velocity anomalies - usually high - oriented along zones containing a high concentration of ray paths) in that area of the model at 9 km depth and 15 km depth. Below 15 km the model rapidly deteriorates as indicated by obvious ray streaking and poor recovery of resolution tests. This LVZ is not present in the velocity model of *Mori et al.* [1996]. A third low velocity body (LVZ3, Figure 7 c-g) is centered ≈7 km to the northeast of the summit and exists from ≈2-3 km b.s.l. to ≈7 km b.s.l. This is the largest LVZ present within the better resolved portions of the model. It appears to be roughly ellipsoidal with the long axis being sub-vertical, and has a maximum horizontal diameter of 6-8 km at about 4 km depth. This feature is also not present in the velocity model of *Mori et al.* [1996]. The exact sizes of these LVZs are difficult to determine and depend greatly upon where one draws the boundary between anomalous and average velocity. However, these three anomalous features are present in roughly the same positions in all models tested and generally vary only in amplitude and constraint.

The small volume of strong low velocity termed LVZ1 above exists only at shallow depths and correlates roughly with the location of the small caldera that formed as a result of the strong June 15 eruption. The relatively shallow depth of LVZ1 probably prohibits it from being a magma body. The pre-eruption existence of thermal springs in this area, coupled with the fact that the 1991 caldera formed just above LVZ1, likely points to it being a highly fractured, highly water-saturated zone of volcaniclastic sediments. This correlates well with the northwest brine system in the "magmatic-hydrothermal" conceptual model of *Delfin et al.* [1996].

The low velocity zone termed LVZ3 above lies just to the northwest of, and is partially intersected by a planar group of earthquakes with an orientation similar to the Sacobia Lineament (SL, discussed in greater detail below). This LVZ is smeared to the southwest and upward along the SL orientation and toward LVZ1. This feature is located at a depth appropriate for the dacitic magma body referred to above and detailed by *Pallister et al.* [1996]. The bottom of this LVZ appears to be at roughly 6-7 km b.s.l., which is the approximate depth where magma mixing is inferred by *Pallister et al.* [1996]. The low velocity smearing that occurs to the southwest (toward the summit) and upward may be the path of least resistance which accommodated the rising of first andesitic magma and then dacitic magma during the June, 1991 eruptions. The large size of this anomaly may be attributed to the magma body actually being composed of

highly fractured, but mostly competent rock with a multitude of sills and dikes cross-cutting its volume [e.g. *Mori et al.*, 1996].

The small, near vertical, pipe-like low velocity anomaly termed LVZ2 above is located at the apparent intersection of the earthquake cluster along the Sacobia Lineament and another cluster possibly representing the depth expression of the Maraunot Fault, which has been mapped as an extension of the regional Iba Fracture Zone. The zone of weakness that would result from the intersection of these two fracture zones would present a convenient path for the ascent of magma from depth. It is plausible that this near vertical "pipe" of low velocities may represent a magma conduit through which mafic magma from a deep source traveled upward to contact the aforementioned dacitic magma body. Alternatively, one or both of the two intermediate to deep LVZs, which lie adjacent to planar zones of earthquakes, may represent weak, highly fractured, fluid filled rock not directly related to magma bodies or conduits.

Hypocenters

The most notable difference between the pre- and post-eruption seismicity is the change from tightly concentrated groups of earthquakes in the pre-eruption group to a more scattered pattern within the post-eruption group. This is probably the effect of the changing stress conditions due to the depressurizing of the magma chamber. The local faults would adjust to this change through a series of slips until a new equilibrium is achieved.

Bautista et al. [1996] noted that composite focal plane solutions from pre- and post-eruption events, fault plane solutions from events occurring during the eruption, and local and regional fault information suggests that movement along these faults preceded, accompanied, and followed the major eruption. There are at least two major fault orientations that intersect at Mt. Pinatubo (Figure 2). An inspection of the relocated hypocenters reveals several features which were not previously apparent. The previously termed "northwest cluster" appears to be composed of two intersecting curved surfaces. The surface trending roughly NW-SE is probably related to the Maraunot Fault. The roughly NE-SW surface, which is located near the rim of the 1991 eruption caldera, may be associated with the Tayawan Fault. The cluster of pre-eruption earthquakes previously termed the "summit cluster" collapsed down from a cloud to a gently curving surface that mimics the orientation of the Maraunot Fault (Figure 2) almost directly above it and is interpreted to be a sequence of earthquakes occurring along this fault at the Pinatubo summit (Figures 8 and 11). The features seen here are consistent with the features found by *Jones et al.* [2001] using a limited set of pre-eruption hypocenters. The occurrence of the earthquakes within this cluster directly preceded the major eruptions, supporting the proposition that rising magma tends to follow the path of least resistance, this path being along pre-existing faults and fractures. Similar ring-fault-like features appear to exist in the post-eruption seismicity with orientations similar to that of the summit cluster (Figure 11); however, these features are difficult to distinguish due to the multitude of overlapping features observed within the complete set of hypocenters.

A band of post-eruption earthquakes roughly oriented northeast-southwest and passing just to the south of the Pinatubo summit is actually composed of at least two sub-parallel planar clusters (Figure 12). These bands are located below the surface expression of the Sacobia Lineament and are here interpreted to be slips occurring along this fault zone at depth in response to the depressurizing of a nearby magma chamber. The improved clarity with which these features are observed in the relocated hypocenters is an indication that at least some improvement in the relative velocities has occurred within the well-resolved model portions. Also, the appearance of these fault-like features in both the pre- and post-eruption seismicity

supports the claim of *Bautista et al.* [1996] that activity on local faults occurred both before and after the June, 1991 eruptions.

The lack of a cluster of pre-eruption earthquakes directly connecting the northeast low velocity zone (LVZ3) to the Pinatubo summit where erupted materials emanated casts some doubt on this feature being the magma chamber feeding the 1991 eruptions. Conversely, the common correlation throughout the model between low velocities and earthquake clusters supports the general conclusion that the subsurface magmatic system is probably composed of numerous magma filled cracks oriented parallel to the two intersecting fault zones discussed above.

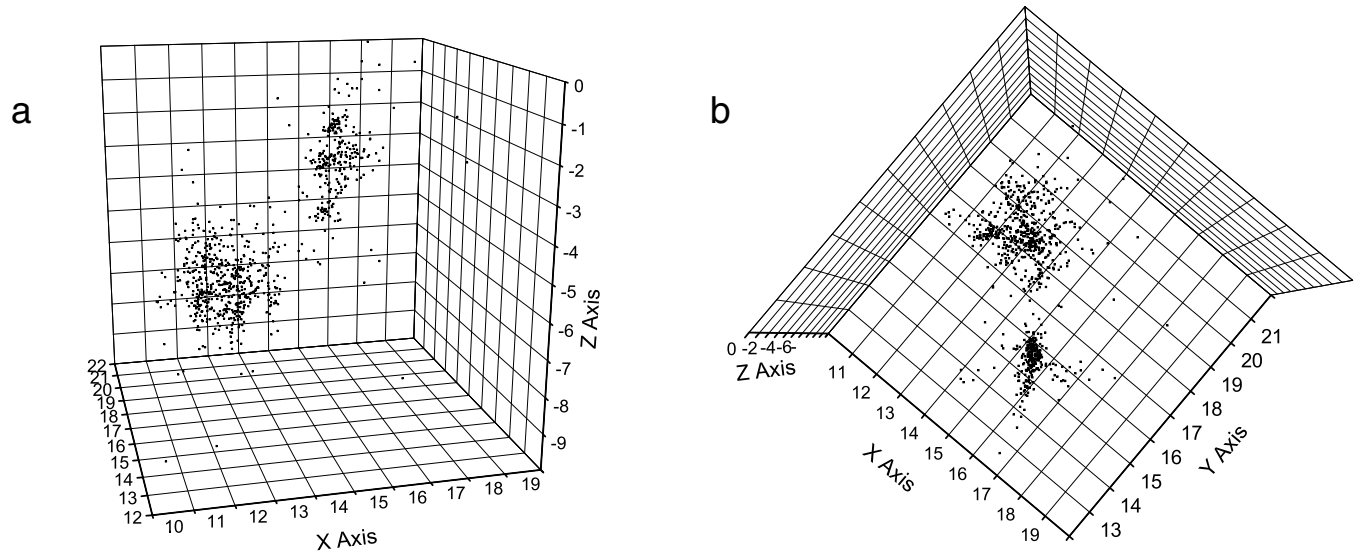

Figure 11. Three-dimensional view of pre-eruption hypocenters showing apparent ring-fault-like features. (a) View of pre-eruption hypocenters looking NNE slightly tilted upward from horizontal. (b) View of pre-eruption hypocenters looking down from a position slightly tilted from vertical to the SE.

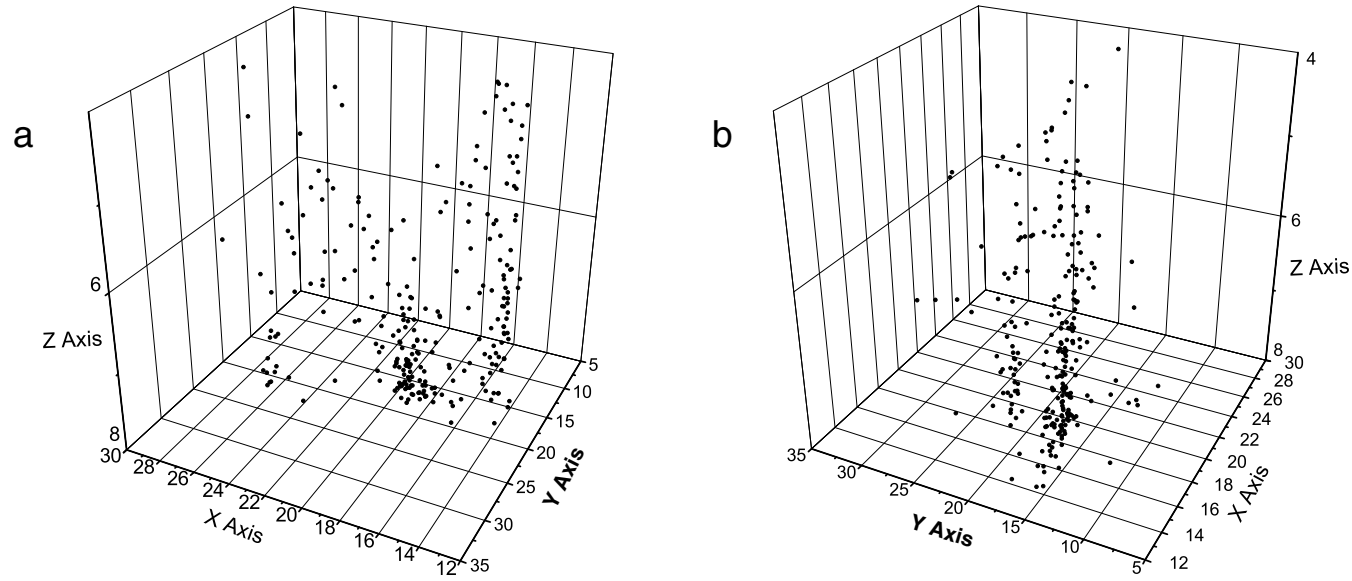

Figure 12. Three-dimensional view of a subset of post-eruption hypocenters showing two sub-parallel, planar features. (a) View of hypocenters from a position normal to the interpreted fault planes (from NW). (b) View of hypocenters from a position along the interpreted fault planes (from SW).

Discussion

The network that was deployed at Pinatubo was aimed at quickly locating and categorizing the events as they occurred, in order to forecast the timing and size of the threatening eruption. To obtain better results from tomography, several changes could be made to the process. In order to image the subsurface at a resolution on the order of one kilometer or less, probably about 25, or more, recording stations within roughly the same area would have been needed. There are some alternatives to a denser station coverage, which might somewhat compensate for the resulting lower ray coverage within the model. The placement of a few stations well outside the "normal" array would provide a greater number of sub-horizontal ray paths, which would help to constrain the velocities within the model. Also, having three components at each station would allow for the recording of more S-wave arrivals which would improve the accuracy of the vertical velocity profile. Another common technique used to constrain near surface velocities is the recording of check shots. Some appropriate number of controlled source shots are recorded by the stations, allowing the 1-D model of the near surface to be more accurately estimated. Any method of constraining the average velocity profile in the area would improve focal depth determinations, improving the accuracy of the ray coverage model. Alternatively, some other means of estimating focal depths would achieve the same results. A re-examination of the digital seismograms to obtain highly accurate and reliable arrival time picks would greatly improve the accuracy of the resulting models. (Picks of unknown origin - likely using program PCEQ - were used here and no independent assessment of their quality could be made.)

Although the network at Pinatubo was not designed for tomography, the resulting data were sufficient to produce a stable inversion result. However, because of the design, significant non-uniqueness is present in the model. The most difficult aspect of the model to constrain was the trade-off between focal depths, origin times, and vertical velocity profile. Despite this non-uniqueness, several aspects of the model are consistent, when the optimum subset of the data are used in the tomography. The existence of low velocity zones (relative to the horizontal average) within models derived from different starting velocities indicates reasonable confidence that these zones are real. The results of the checkerboard testing verify the ability of the tomography to resolve structures of this size within the volume of good ray coverage. Also, the apparent improvement of hypocenter locations, indicated by the resolving of fault-like patterns of seismicity further reinforces the believability of the results.

The low velocity zones described here are interpreted to be a part of a large "magmatic-hydrothermal" system, similar to the conceptual model of *Delfin et al.* [1996]. It is doubtful that all three of the noted LVZs are magma chambers, but it seems likely that each of them represents some zone of weakness that may have served as a path for magma ascent. The near surface zone (LVZ1) probably represents a zone of water saturated, highly fractured rock and is located just below the 1991 eruption caldera. The pre-eruption hypocenters show patterns of ring faulting around this zone. A similar zone of low velocity was found by *Mori et al.* [1996]. The deep low velocity zone (LVZ2), located at the intersection of two regional fracture zones, possibly represents the path of mafic magma ascent toward the cooler dacitic body at roughly 10 km depth [*Pallister et al.*, 1996 and *Endo et al.*, 1996]. If this LVZ can be spatially linked to the deep, long period seismicity that has been recorded both before [*White*, 1996] and after the 1991 eruption, this would strengthen the link to a deep, mafic source. The third significant zone (LVZ3), appears to be related to the regional Sacobia Lineament. A large number of post-eruption earthquakes were located along the trend of this lineament and LVZ3 is located

alongside this band of earthquakes. It is possible that a section of this planar zone of weakness is serving as a path of least resistance for periodic magma ascent. The two deeper LVZs (2 and 3) are not found in the previous tomography of *Mori et al.* [1996]; and the LVZ at 6-11 km found in the previous tomography is not found in the present study. The three low velocity zones discussed here are consistent with the results of previous studies of the 1991 Mt. Pinatubo eruption. Testing shows that the results of the tomography are reasonable. Also, the correlation between the final velocity model and the improved hypocenters is a positive sign. However, the definite existence of non-uniqueness in the model leaves open a number of possible explanations for the existence of these features.

References

Aki, K., Christoffersson, A., and Husebye, E.S., 1977, Determination of the three dimensional seismic structure of the lithosphere: J. Geophys. Res., **82**, 277-296.

Aki, K., and Lee, W.H.K., 1976, Determination of three-dimensional velocity anomalies under a seismic array using first P-arrival times from local earthquakes, 1, A homogeneous initial model: J. Geophys. Res., **81**, 4381-4399.

Bautista, B.C., Bautista, Ma. L.P., Stein, R.S., Barcelona, E.S., Punongbayan, R.S., Laguerta, E.P., Rasdas, A.R., Ambubuyog, G., and Amin, E.Q., 1996, Relationship of regional and local structures to Mount Pinatubo activity: In: Newhall, C.G., Punongbayan, R.S. (Eds.), Fire and Mud: Eruptions and Lahars of Mount Pinatubo, Philippines. PHIVOLCS, Quezon City, University of Washington Press, Seattle, WA, pp. 351-370.

Benz, H.M., Chouet, B.A., Dawson, P.B., Lahr, J.C., Page, R.A., and Hole, J.A., 1996, Three-dimensional P and S wave velocity structure of Redoubt Volcano, Alaska, J. Geophys. Res., **101**, 8111-8128.

Dawson, P.B., Chouet, B.A., Okubo, P.G., Villaseñor, A., and Benz, H.M., 1999, Three-dimensional velocity structure of the Kilauea caldera, Hawaii: Geophys. Res. Lett., **26**, 2805-2808.

deBoer, J.Z., Odom, L.A., Ragland, P.C., Snider, F.G., and Tilford, N.R., 1980, The Bataan orogene: Eastward subduction, tectonic rotations, and volcanism in the western Pacific (Philippines): Tectonophysics, **67**, 305-317.

Delfin, F.G., Jr., Villarosa, H.G., Layugan, D.B., Clemente, V.C., Candelaria, M.R., and Ruaya, J.R., 1996, Geothermal exploration of the pre-1991 Mount Pinatubo hydrothermal system: In: Newhall, C.G., Punongbayan, R.S. (Eds.), Fire and Mud: Eruptions and Lahars of Mount Pinatubo, Philippines. PHIVOLCS, Quezon City, University of Washington Press, Seattle, WA, pp. 197-212.

Eberhart-Phillips, D., 1993, Local earthquake tomography: Earthquake source regions: In: Iyer, H.M., and Hirahira, K., (Eds.), Seismic tomography: Theory and practice. London, Chapman and Hall, 613-643.

Endo, E.T, Murray, T.L., and Power, J.A., 1996, A comparison of preeruption real-time seismic amplitude measurements for eruptions at Mount St. Helens, Redoubt Volcano, Mount Spurr, and Mount Pinatubo: In: Newhall, C.G., Punongbayan, R.S. (Eds.), Fire and Mud: Eruptions and Lahars of Mount Pinatubo, Philippines. PHIVOLCS, Quezon City, University of Washington Press, Seattle, WA, pp. 233-247.

Harlow, D.H., Power, J.A., Laquerta, E.P., Ambubuyog, G., White, R.A., and Hoblitt, R.P., 1996, Precursory seismicity and forecasting of the June 15, 1991, eruption of Mount Pinatubo: In: Newhall, C.G., Punongbayan, R.S. (Eds.), Fire and Mud: Eruptions and Lahars of Mount Pinatubo, Philippines. PHIVOLCS, Quezon City, University of Washington Press, Seattle, WA, pp. 285-305.

Hole, J.A., 1992, Nonlinear high-resolution three-dimensional seismic travel time tomography, J. Geophys. Res., **97**, 6553-6562.

Hole, J.A., and Zelt, B.C., 1995, 3-D finite difference reflection traveltimes: Geophys. J. Int., **121**, 427-434.

Hole, J.A., Brocher, T.M., Klemperer, S.L., Parsons, T., Benz, H.M., and Furlong, K.P., 2000, Three-dimensional seismic velocity structure of the San Francisco Bay area: J. Geophys. Res., **105**, 13,859-13,874.

Humphreys, E., and Clayton, R.W., 1988, Adaptation of back projection tomography to seismic travel time problems: J. Geophys. Res., **93**, 1073-1085.

Iversen, E.S. Jr., and Lees, J.M., 1996, A statistical technique for validating velocity models: Bull. of the Seis. Soc. of Amer., **86**, 1853-1862.

Jones, J.P., Thurber, C.H., and Lutter, W.J., 2001, High precision location of pre-eruption seismicity at Mount Pinatubo, Philippines, 30 May-3 June, 1991: Phys. of the Earth and Plan. Inter., **123**, 221-232.

Lahr, J.C., 1989, HYPOELLIPSE/Version 2.0: A computer program for determining local earthquakes hypocentral parameters, magnitude, and first-motion pattern: U.S. Geological Survey Open-File Report,**89-116**, 92 p.

Lees, J.M., 1992, The magma system of Mount St. Helens: non-linear high-resolution P-wave tomography: Journal of Volc. and Geotherm. Res., **53**, 103-116.

Lees, J.M. and Crosson, R.S., 1989, Tomographic inversion for three-dimensional velocity structure at Mount St. Helens using earthquake data: J. Geophys. Res., **94**, 5716-5728.

Lockhart, A.B., Marcial, S., Ambubuyog, G., Laguerta, E.P., and Power, J.A., 1996, Installation, operation, and technical specifications of the first Mount Pinatubo telemetered seismic network: In: Newhall, C.G., Punongbayan, R.S. (Eds.), Fire and Mud: Eruptions and Lahars of Mount Pinatubo, Philippines. PHIVOLCS, Quezon City, University of Washington Press, Seattle, WA, pp. 215-224.

Michelena, R.J., and Harris, J.M., 1991, Tomographic traveltime inversion using natural pixels: Geophysics, **56**, 635-644.

Michelini, A., and McEvilly, T.V., 1991, Seismological studies at Parkfield: I. Simultaneous inversion for velocity structure and hypocenters using cubic B-splines parameterization: Bull. of the Seis. Soc. of Amer., **81**, 524-552.

Mori, J., Eberhart-Phillips, D., and Harlow, D.H., 1996, Three-dimensional velocity structure at Mt. Pinatubo: resolving magma bodies and earthquake hypocenters: In: Newhall, C.G., Punongbayan, R.S. (Eds.), Fire and Mud: Eruptions and Lahars of Mount Pinatubo, Philippines. PHIVOLCS, Quezon City, University of Washington Press, Seattle, WA, pp. 371-382.

Newhall, C.G., Daag, A.S., Delfin, F.G.Jr., Hoblitt, R.P., McGeehin, J., Pallister, J.S., Regalado, Ma. T.M., Rubin, M., Tubianosa, B.S., Tamayo, R.A., Jr., and Umbal, J.V., 1996, Eruptive history of Mount Pinatubo: In: Newhall, C.G., Punongbayan, R.S. (Eds.), Fire and Mud: Eruptions and Lahars of Mount Pinatubo, Philippines. PHIVOLCS, Quezon City, University of Washington Press, Seattle, WA, pp. 165-196.

Pallister, J.S., Hoblitt, R.P., Meeker, G.P., Knight, R.J., and Siems, D.F., 1996, Magma mixing at Mount Pinatubo: Petrographic and chemical evidence from the 1991 deposits: In: Newhall, C.G., Punongbayan, R.S. (Eds.), Fire and Mud: Eruptions and Lahars of Mount Pinatubo, Philippines. PHIVOLCS, Quezon City, University of Washington Press, Seattle, WA, pp. 687-731.

Thurber, C.H., 1983, Earthquake locations and three-dimensional crustal structure in the Coyote Lake area, central California: J. Geophys. Res., **88**, 8226-8236.

Thurber, C.H., 1984, Seismic detection of the summit magma complex of Kilauea Volcano, Hawaii: Science, **223**, 165-167.

Thurber, C.H., 1992, Hypocenter-velocity structure coupling in local earthquake tomography: Phys. of the Earth and Plan. Inter., **75**, 55-62.

Vidale, J.E., 1990, Finite-difference calculation of traveltimes in three-dimensions: Gephysics, **55**, 521-526.

Villaseñor, A., Benz, H.M., Filippi, L., De Luca, G., Scarpa, R., Patanè, G., and Vinciguerra, S., 1998, Three-dimensional P-wave velocity structure of Mt. Etna, Italy: Geophys. Res. Lett., **25**, 1975-1978.

Wessel, P., and W. H. F. Smith, 1998, New, improved version of Generic Mapping Tools released: EOS Trans. Amer. Geophys. U., **79**, 579.

White, R.A., 1996, Precursory deep long-period earthquakes at Mount Pinatubo: Spatio-temporal link to a basalt trigger: In: Newhall, C.G., Punongbayan, R.S. (Eds.), Fire and Mud: Eruptions and Lahars of Mount Pinatubo, Philippines. PHIVOLCS, Quezon City, University of Washington Press, Seattle, WA, pp. 307-326.

Zelt, C.A., 1998, Lateral velocity resolution from three-dimensional seismic refraction data: Geophys. Journ. Int., **135**, 1101-1112.

Appendix

Horizontal sections through the checkerboard models.

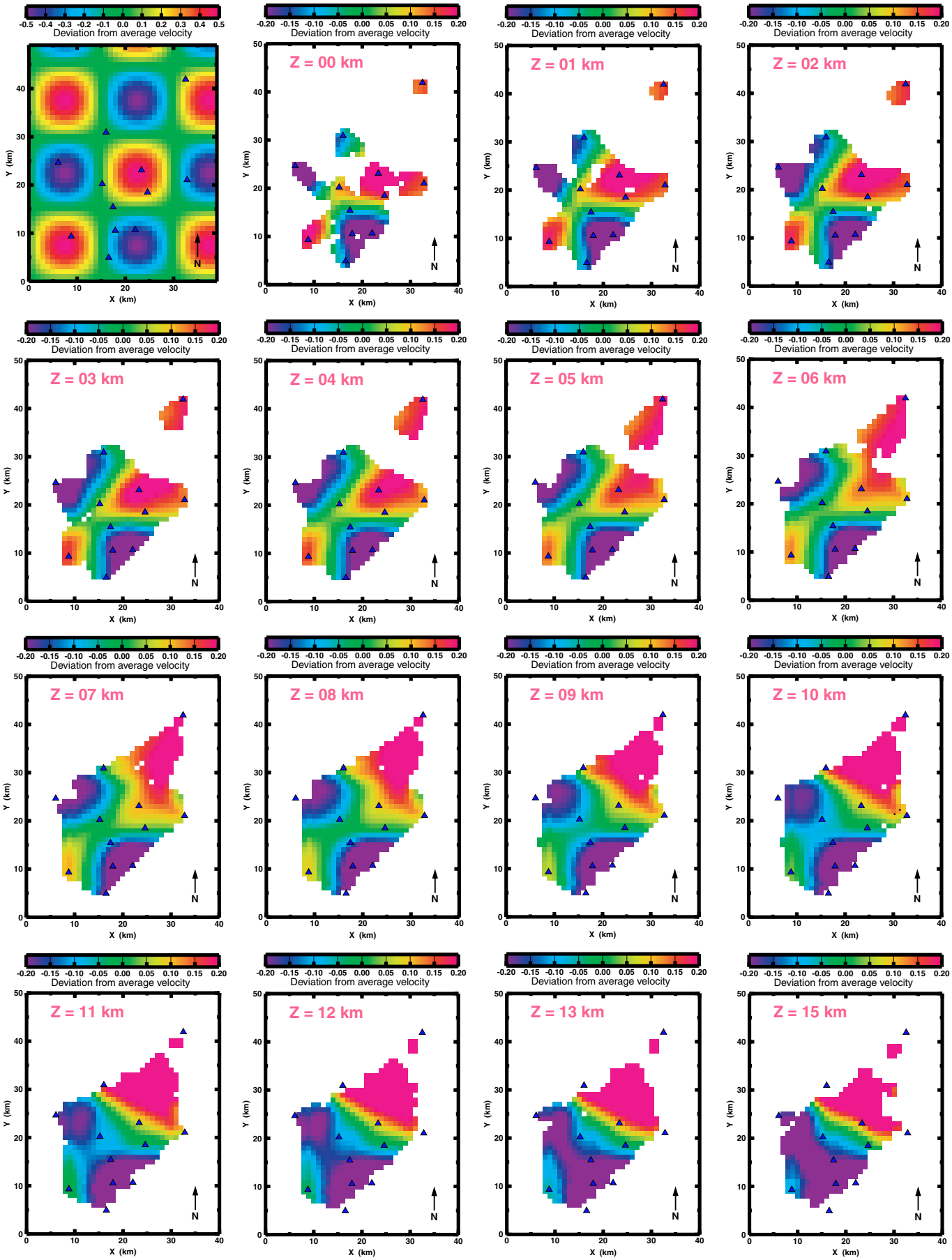

Figure A1. Depth slices through reconstructed 15 km checkerboard model (pattern configuration 1).

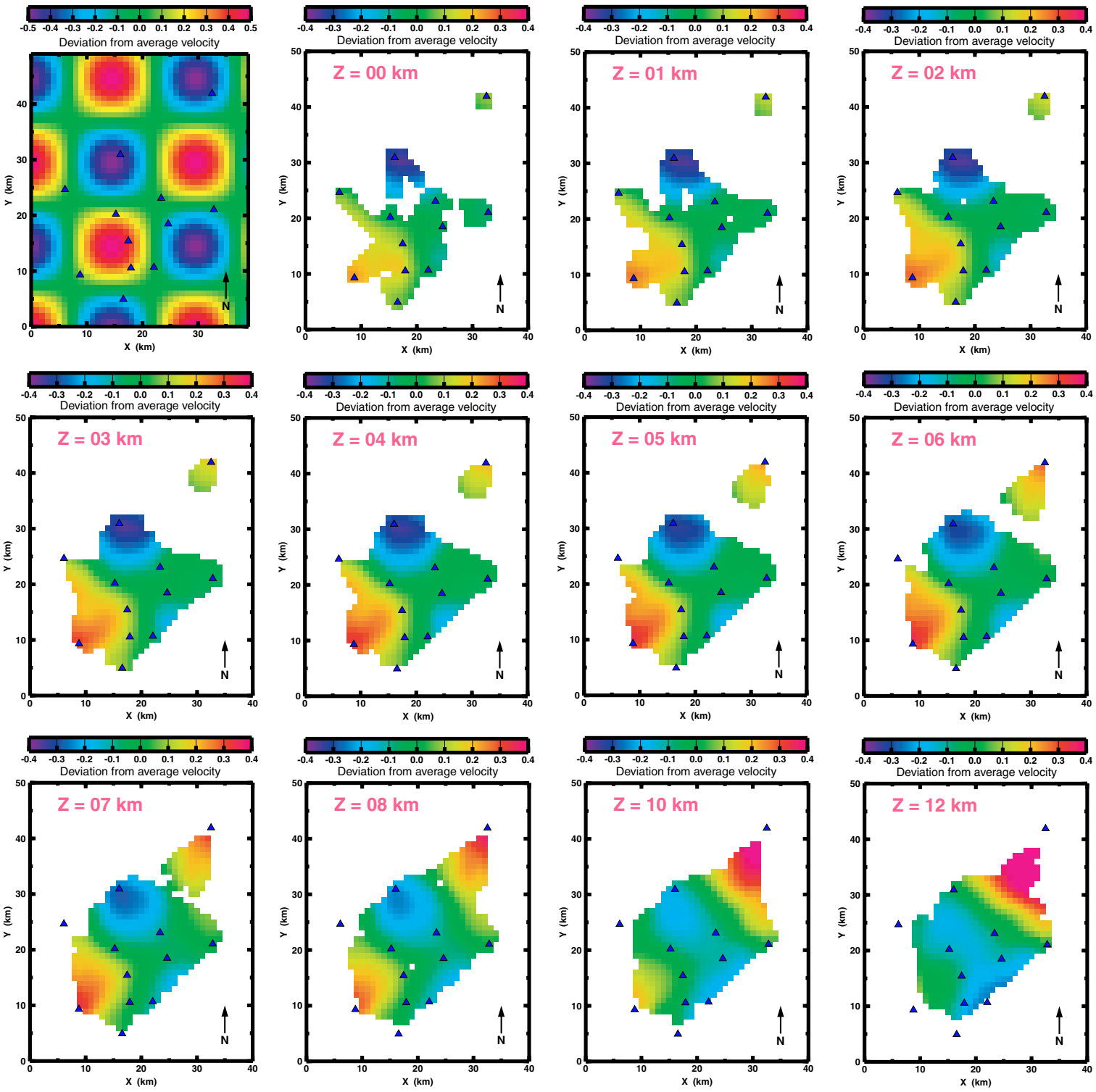

Figure A2. Depth slices through reconstructed 15 km checkerboard model (pattern configuration 2).

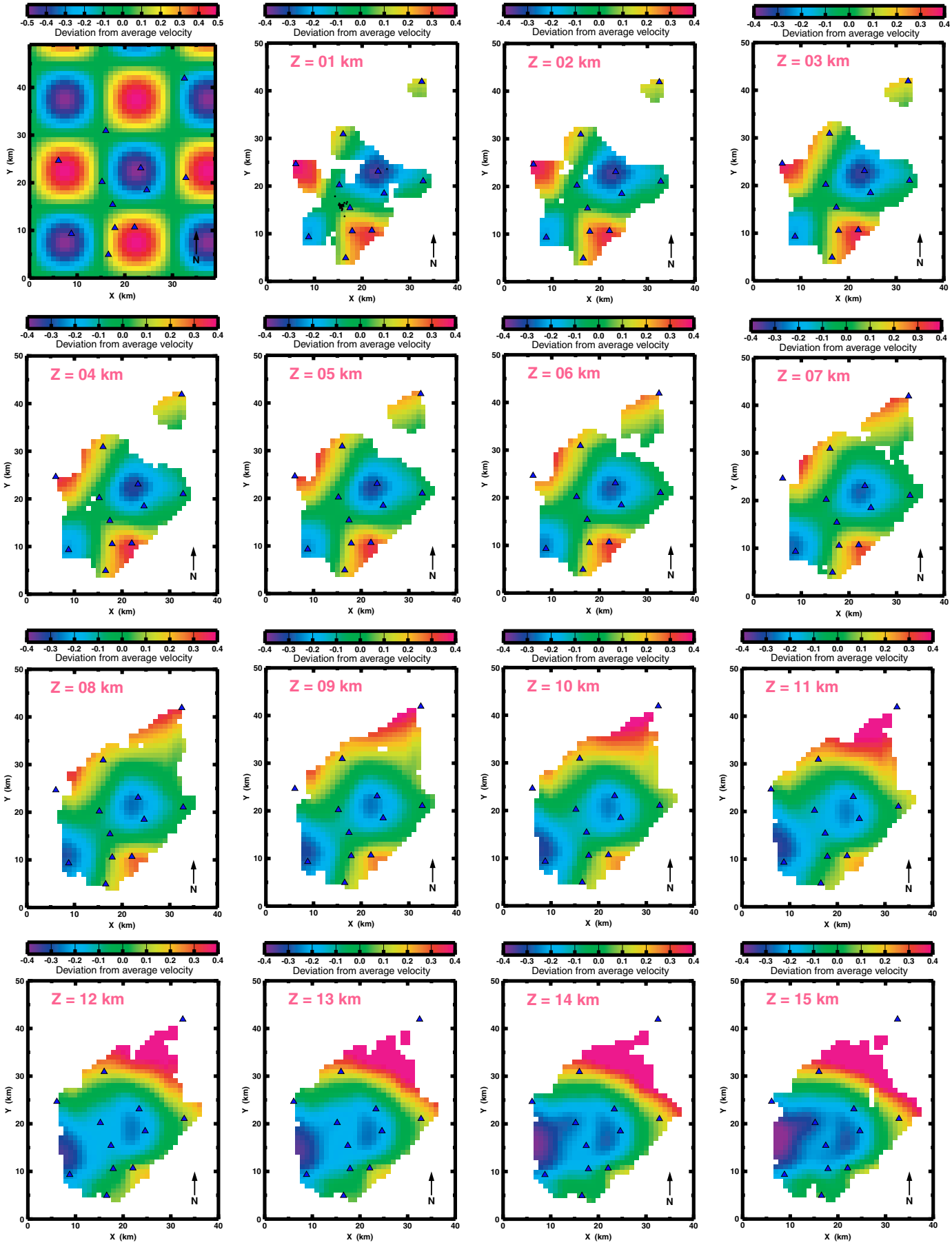

Figure A3. Depth slices through reconstructed 15 km checkerboard model (pattern configuration 3).

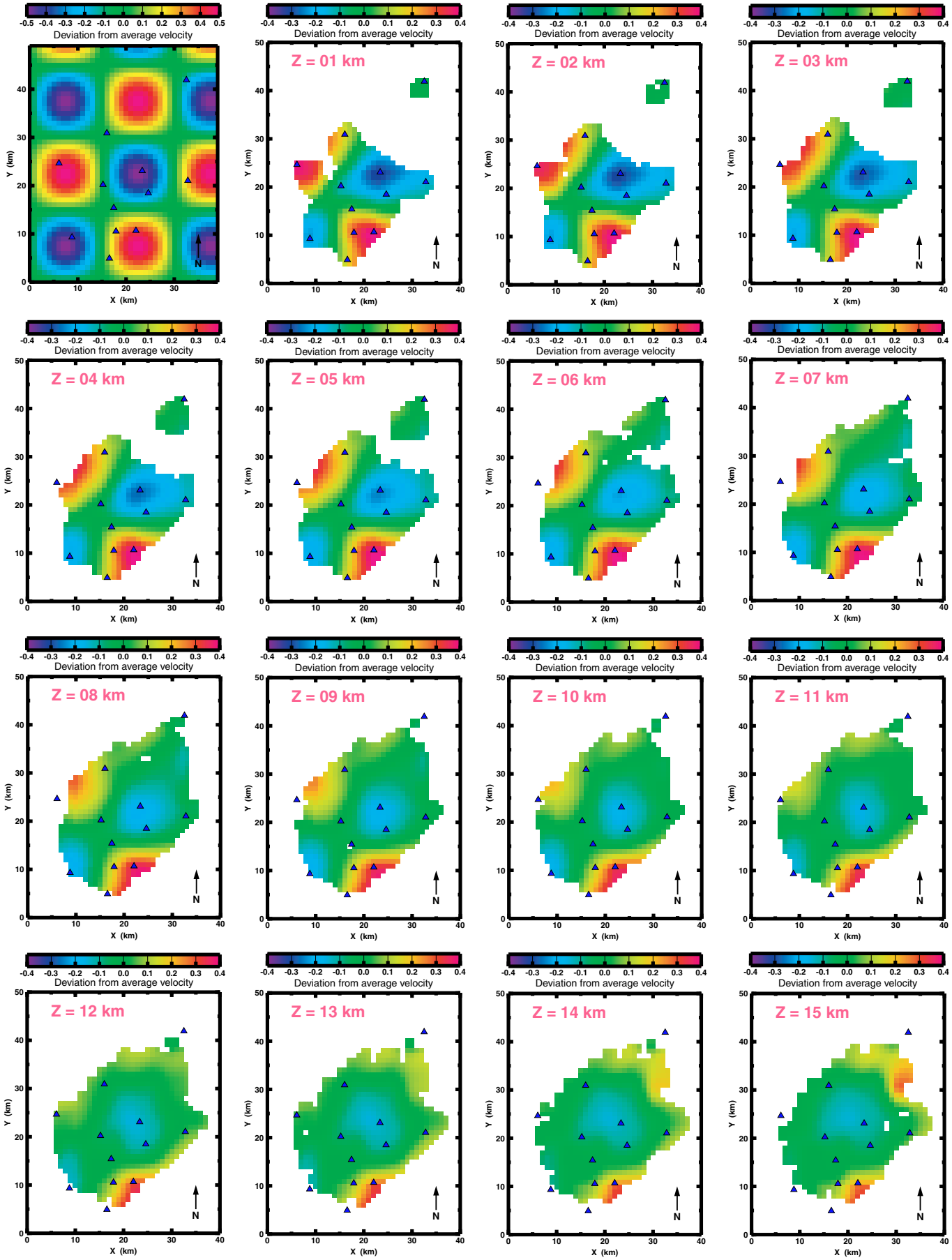

Figure A4. Depth slices through reconstructed 15 km checkerboard model (pattern configuration 4).

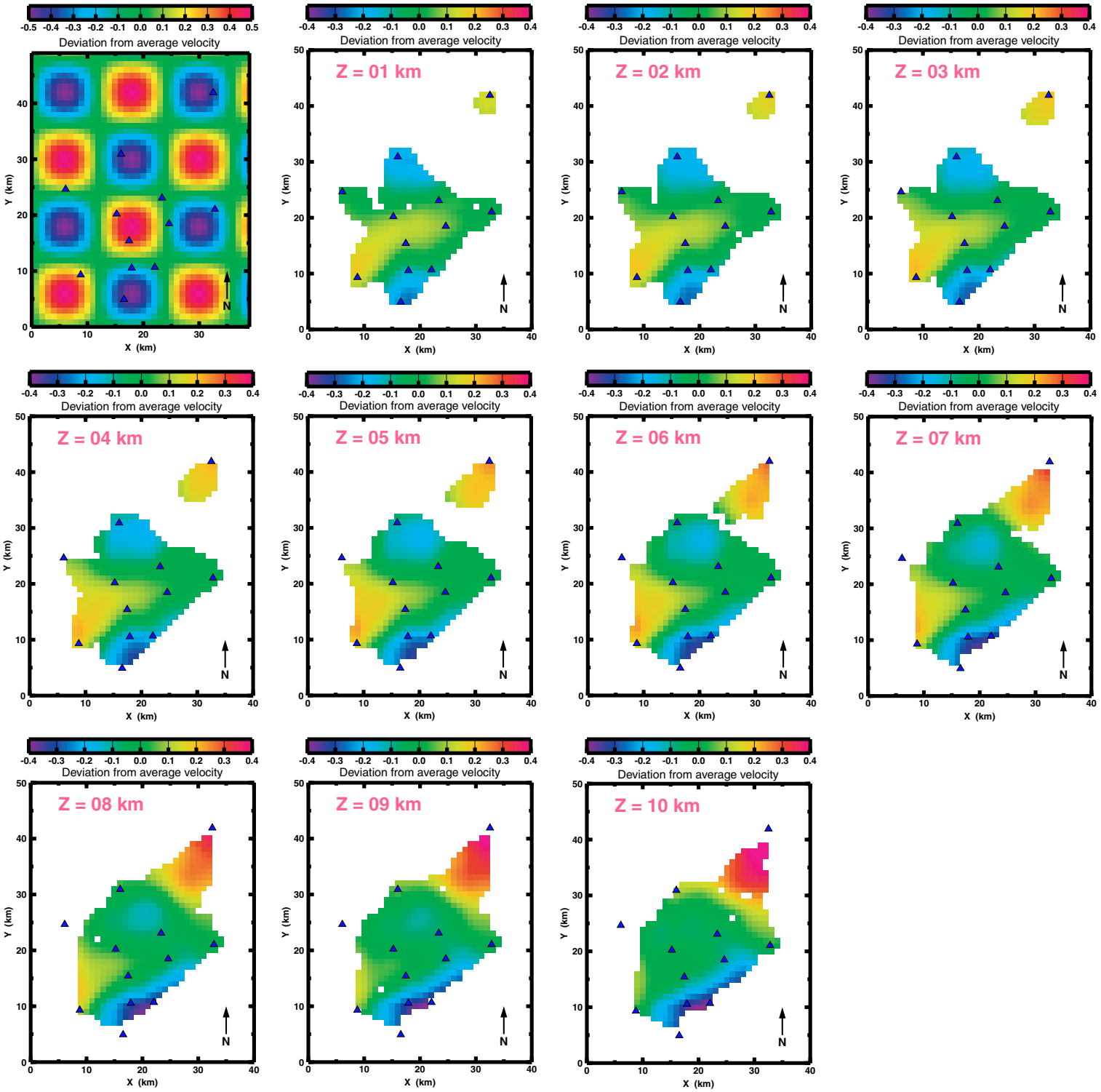

Figure A5. Depth slices through reconstructed 12 km checkerboard model (pattern configuration 1).

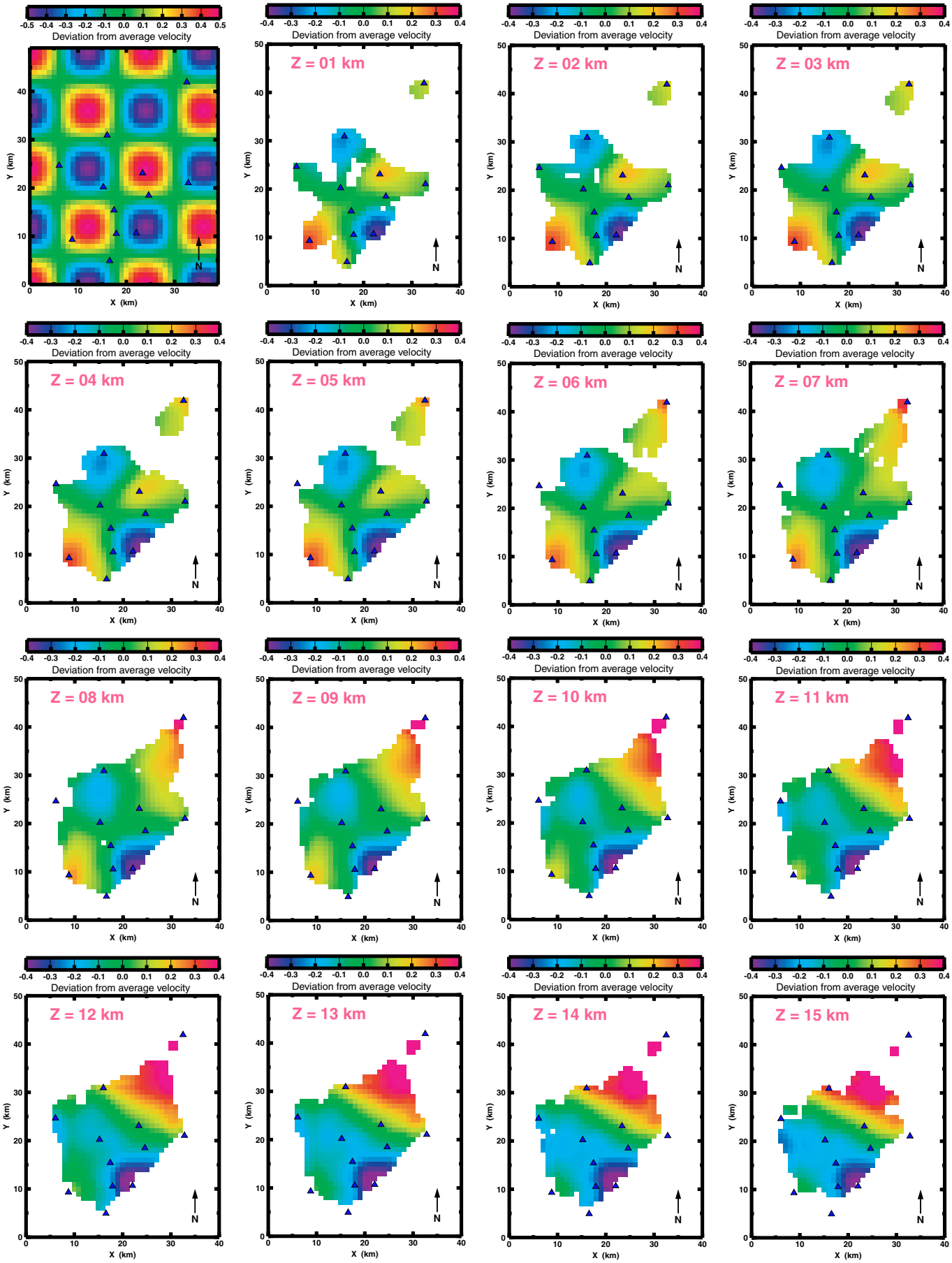

Figure A6. Depth slices through reconstructed 12 km checkerboard model (pattern configuration 2).

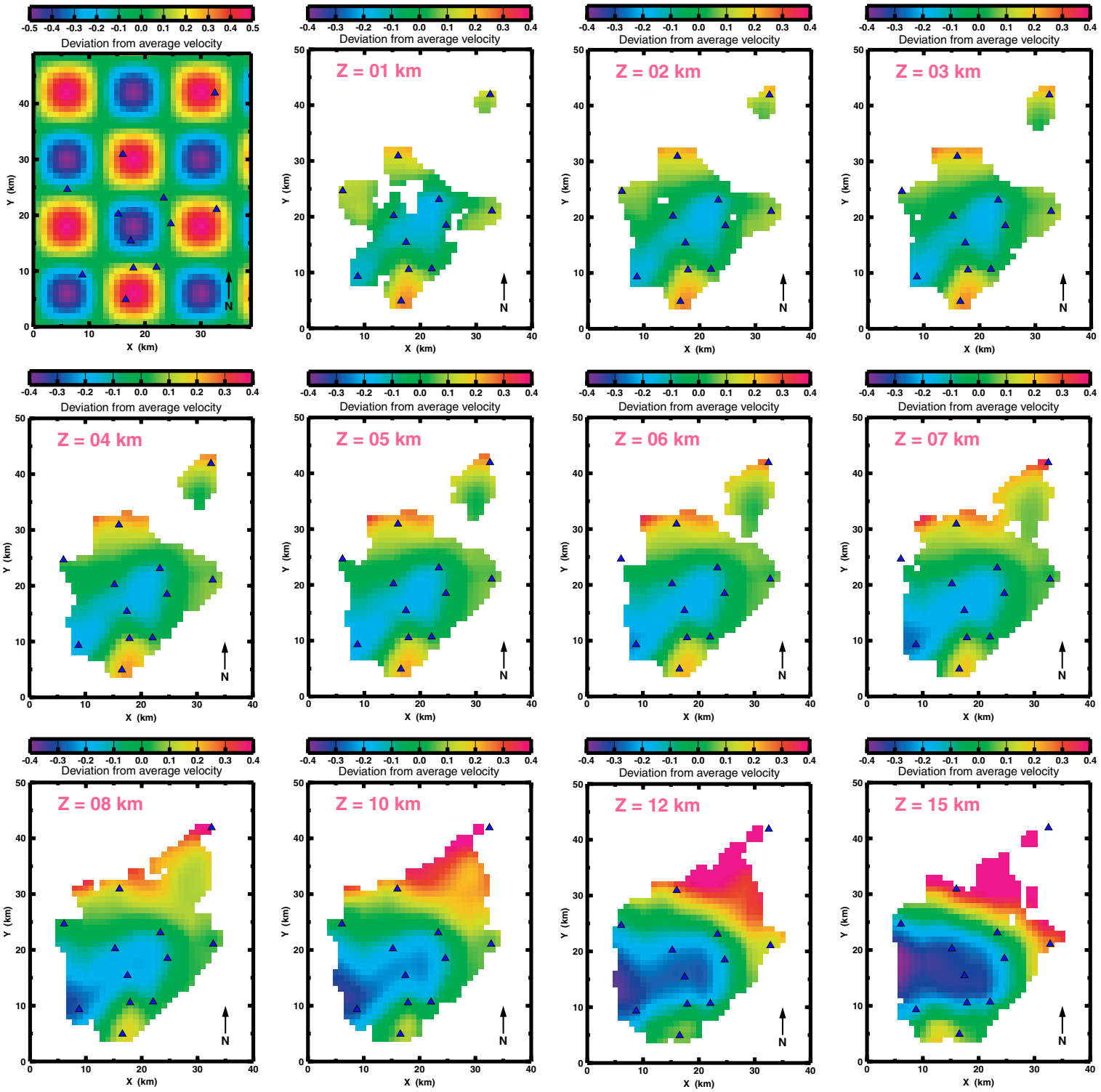

Figure A7. Depth slices through reconstructed 12 km checkerboard model (pattern configuration 3).

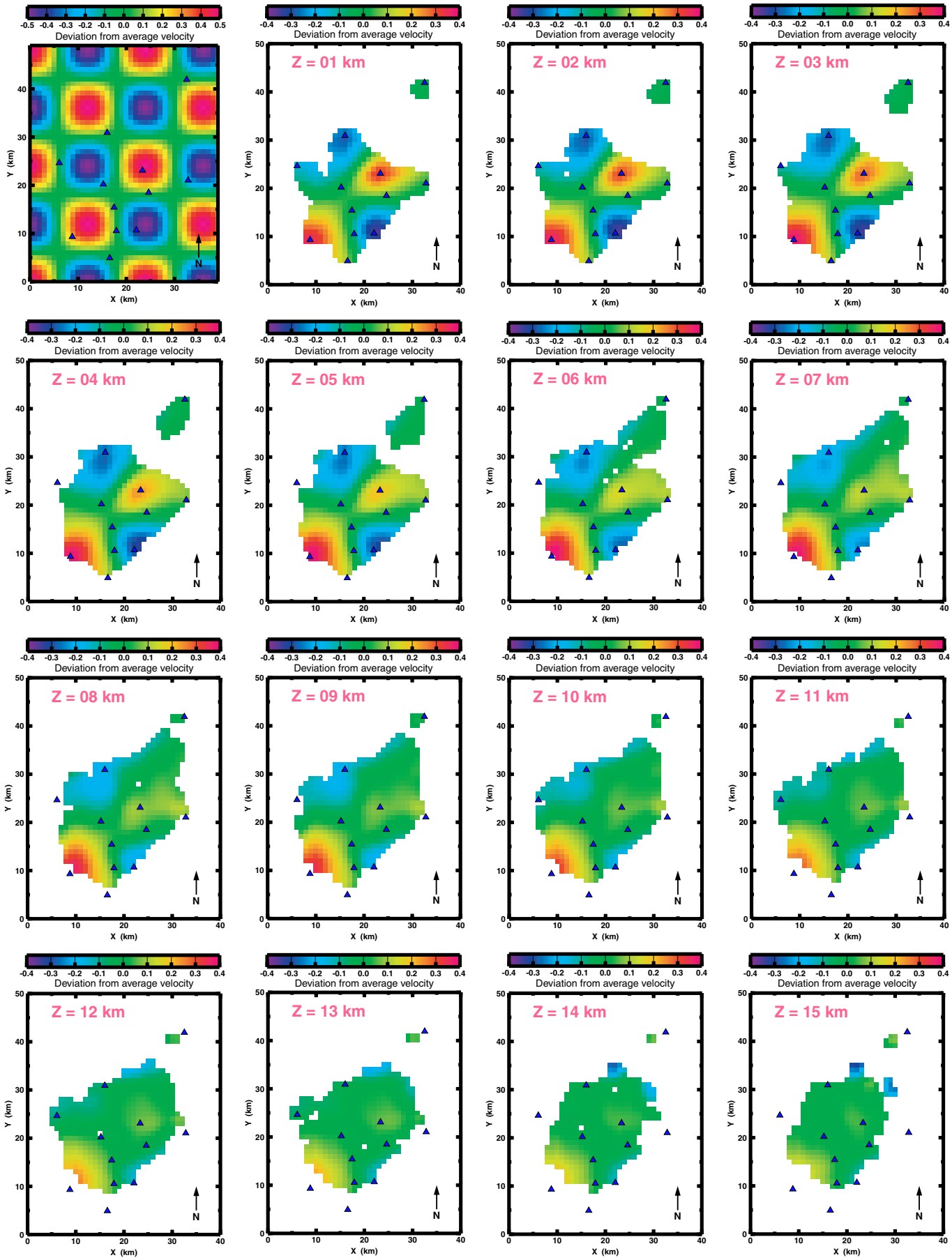

Figure A8. Depth slices through reconstructed 12 km checkerboard model (pattern configuration 4).

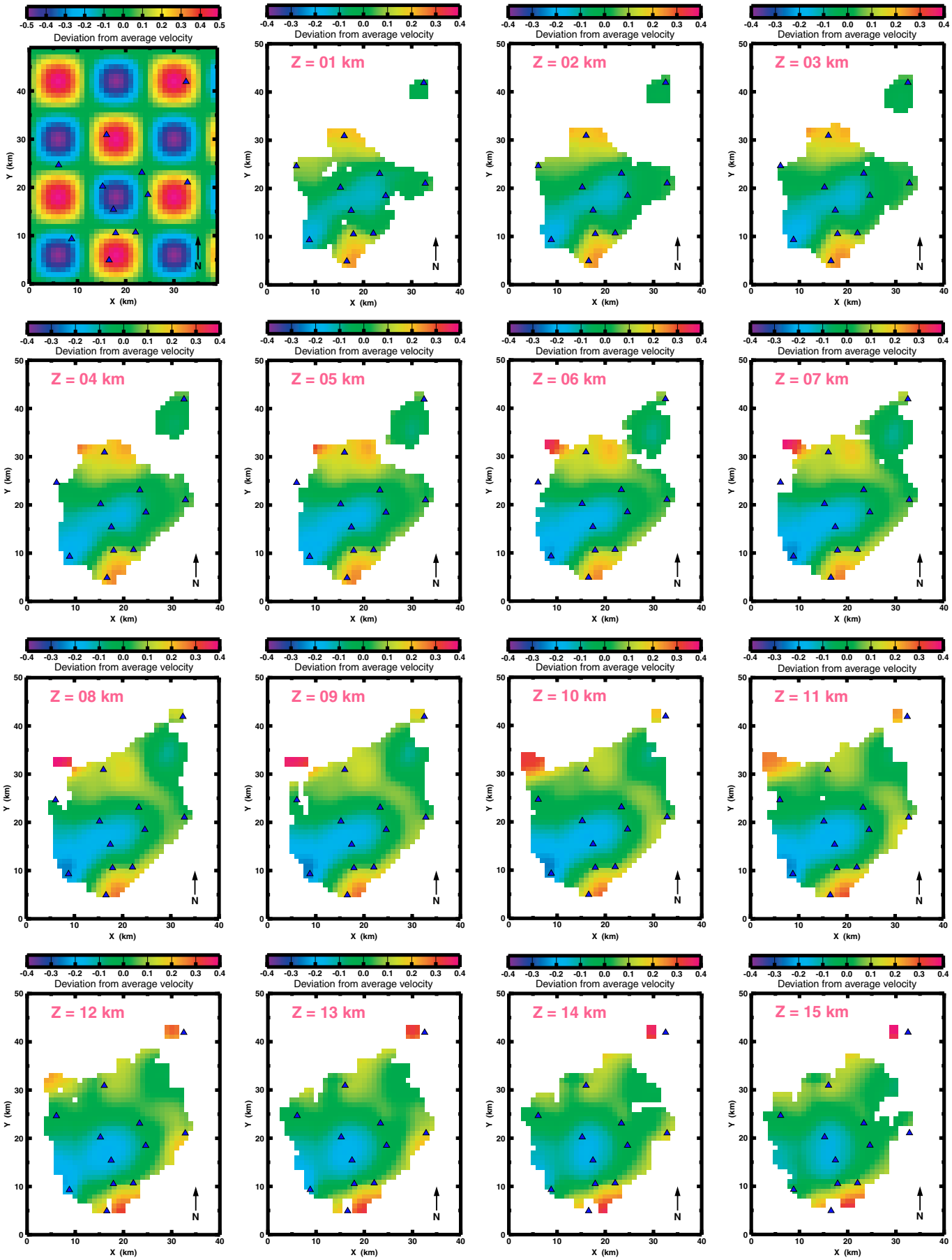

Figure A9. Depth slices through reconstructed 12 km checkerboard model (pattern configuration 5).

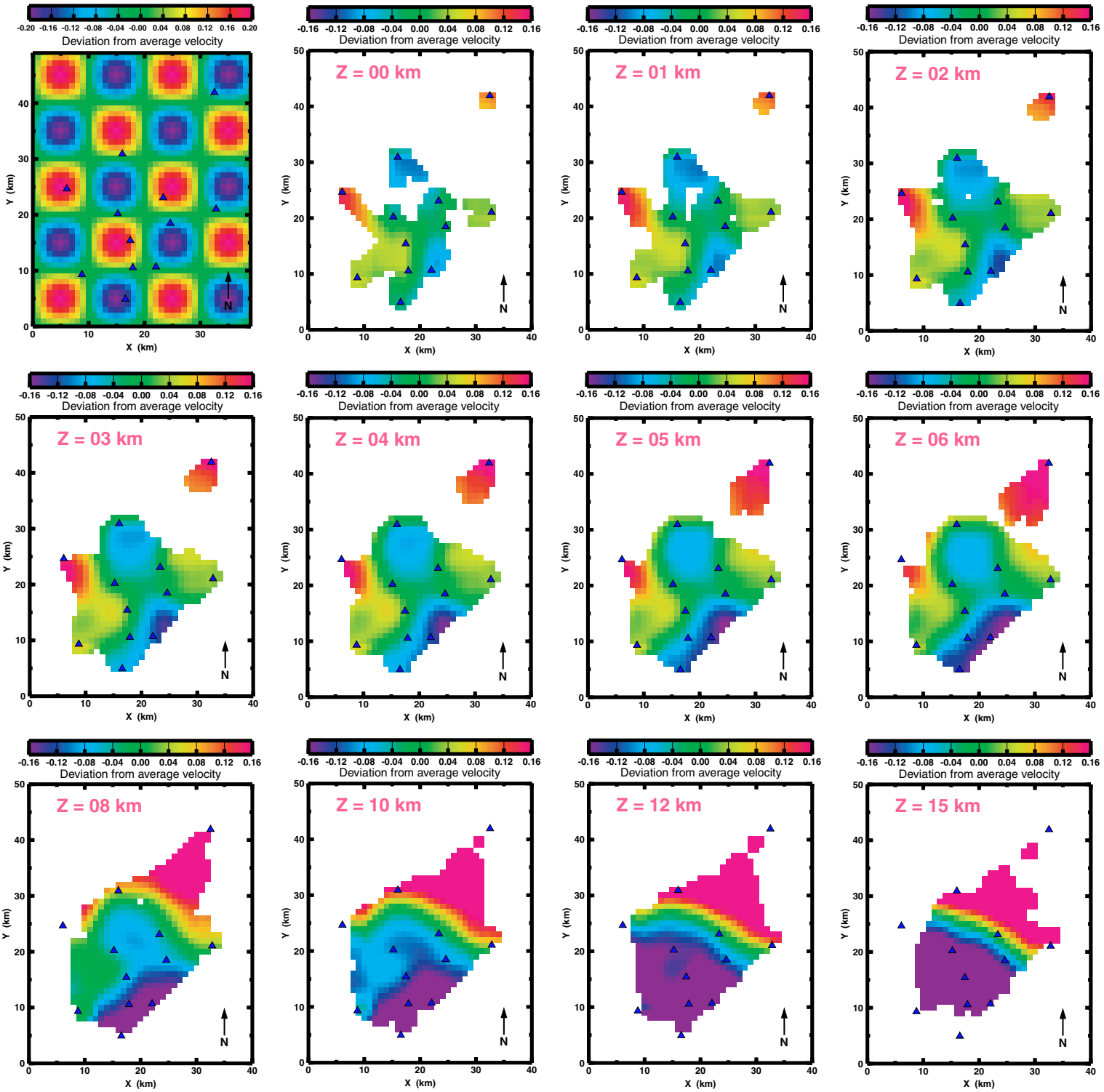

Figure A10. Depth slices through reconstructed 10 km checkerboard model (pattern configuration 1).

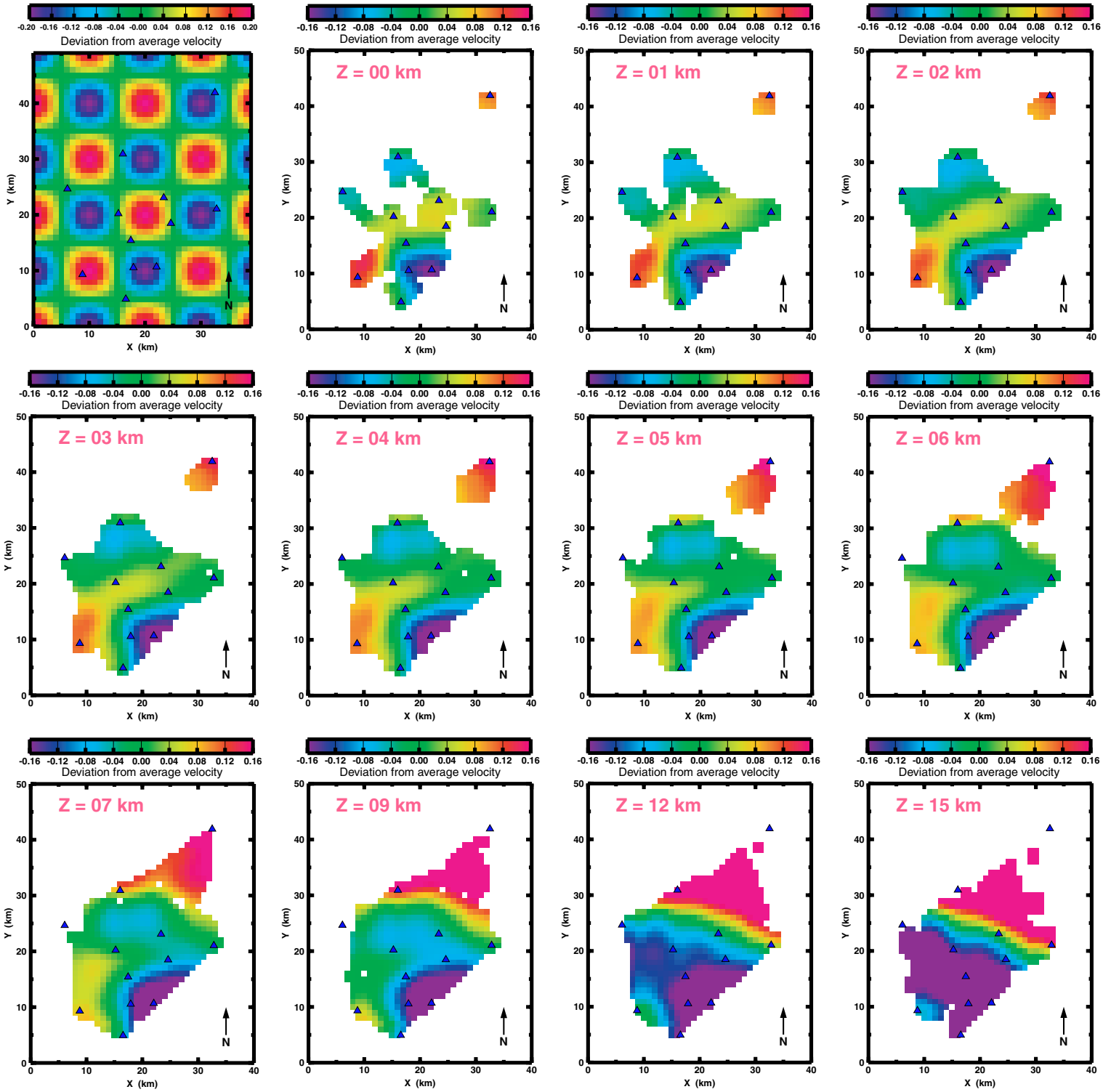

Figure A11. Depth slices through reconstructed 10 km checkerboard model (pattern configuration 2).

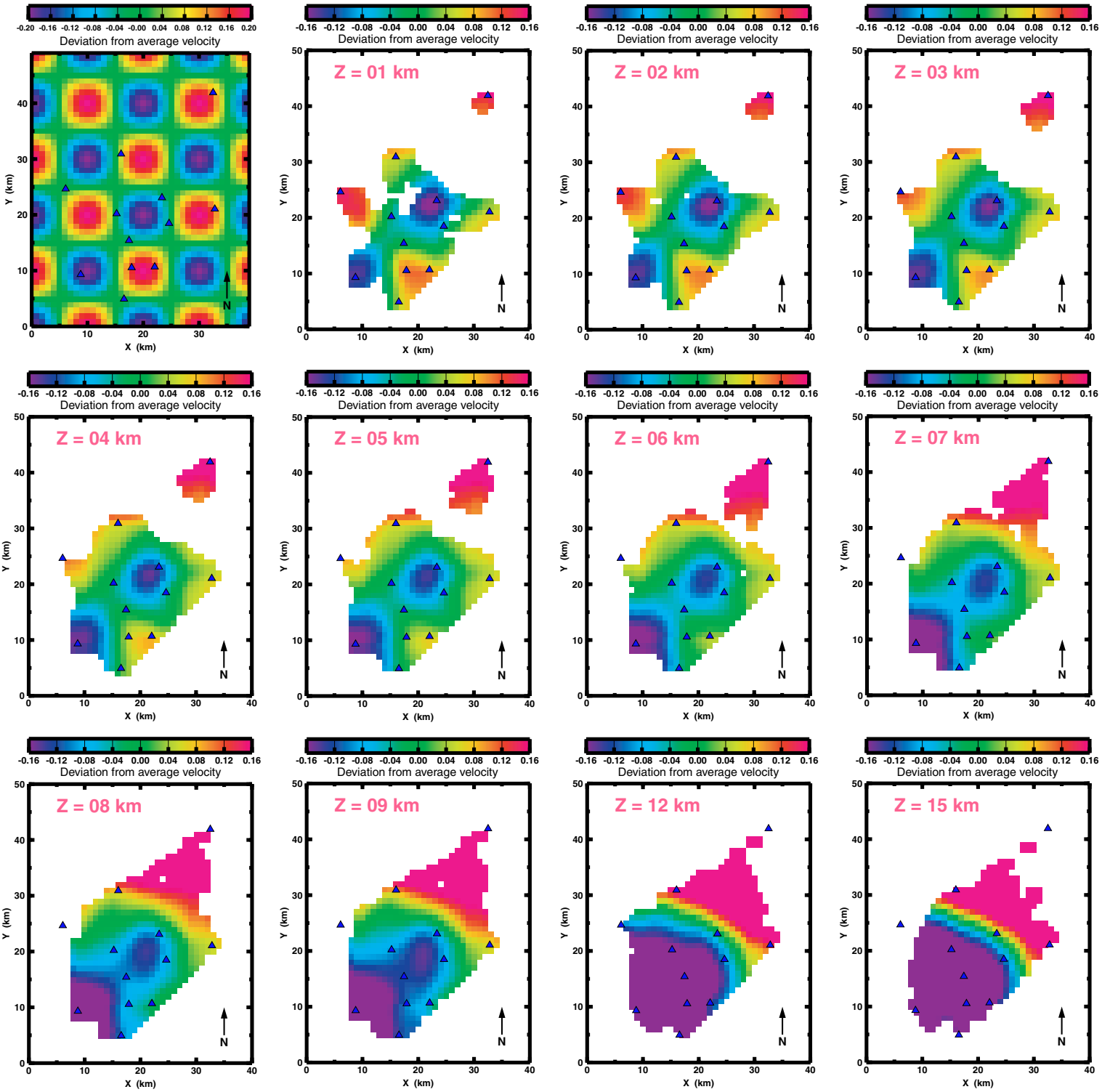

Figure A12. Depth slices through reconstructed 10 km checkerboard model (pattern configuration 3).

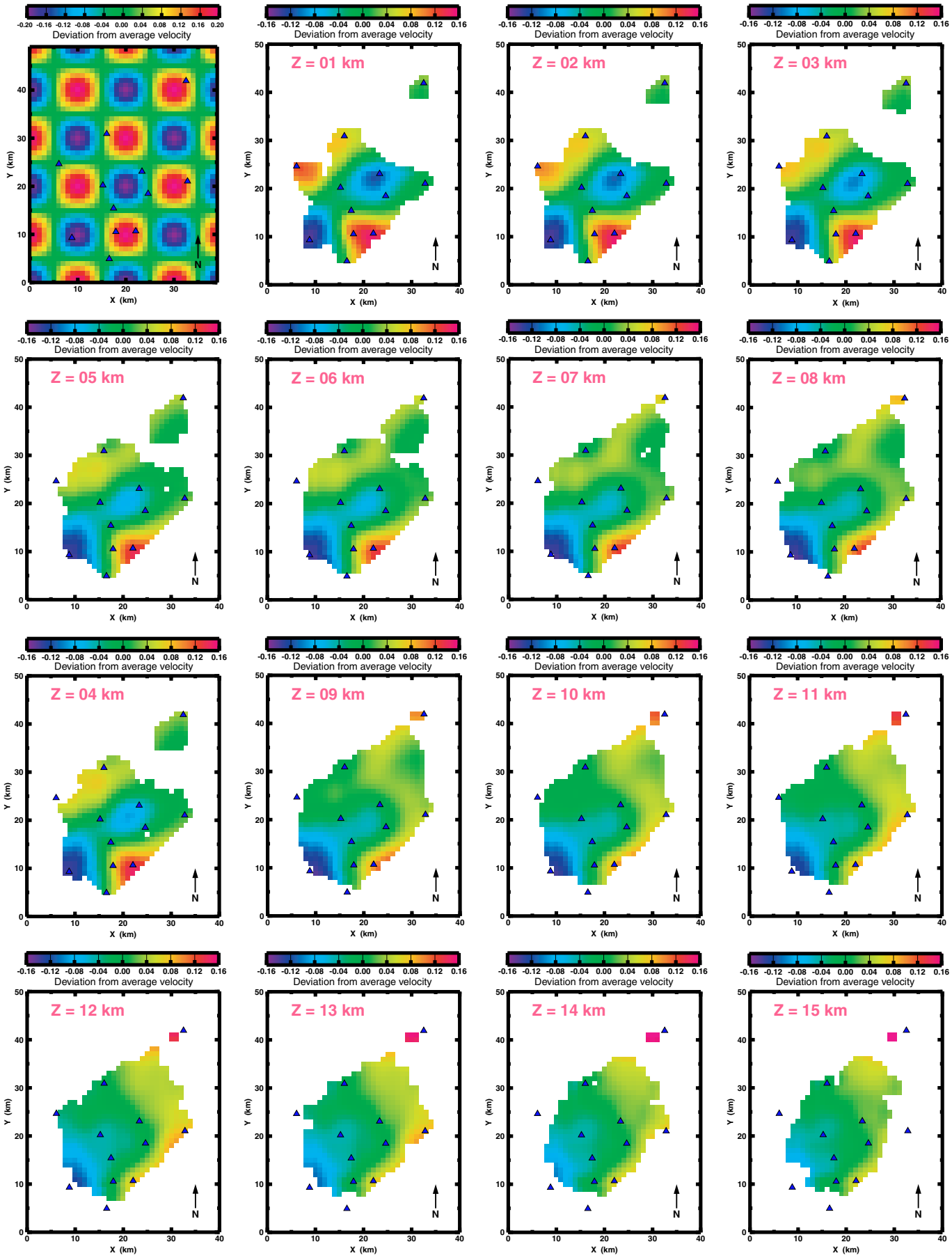

Figure A13. Depth slices through reconstructed 10 km checkerboard model (pattern configuration 4).

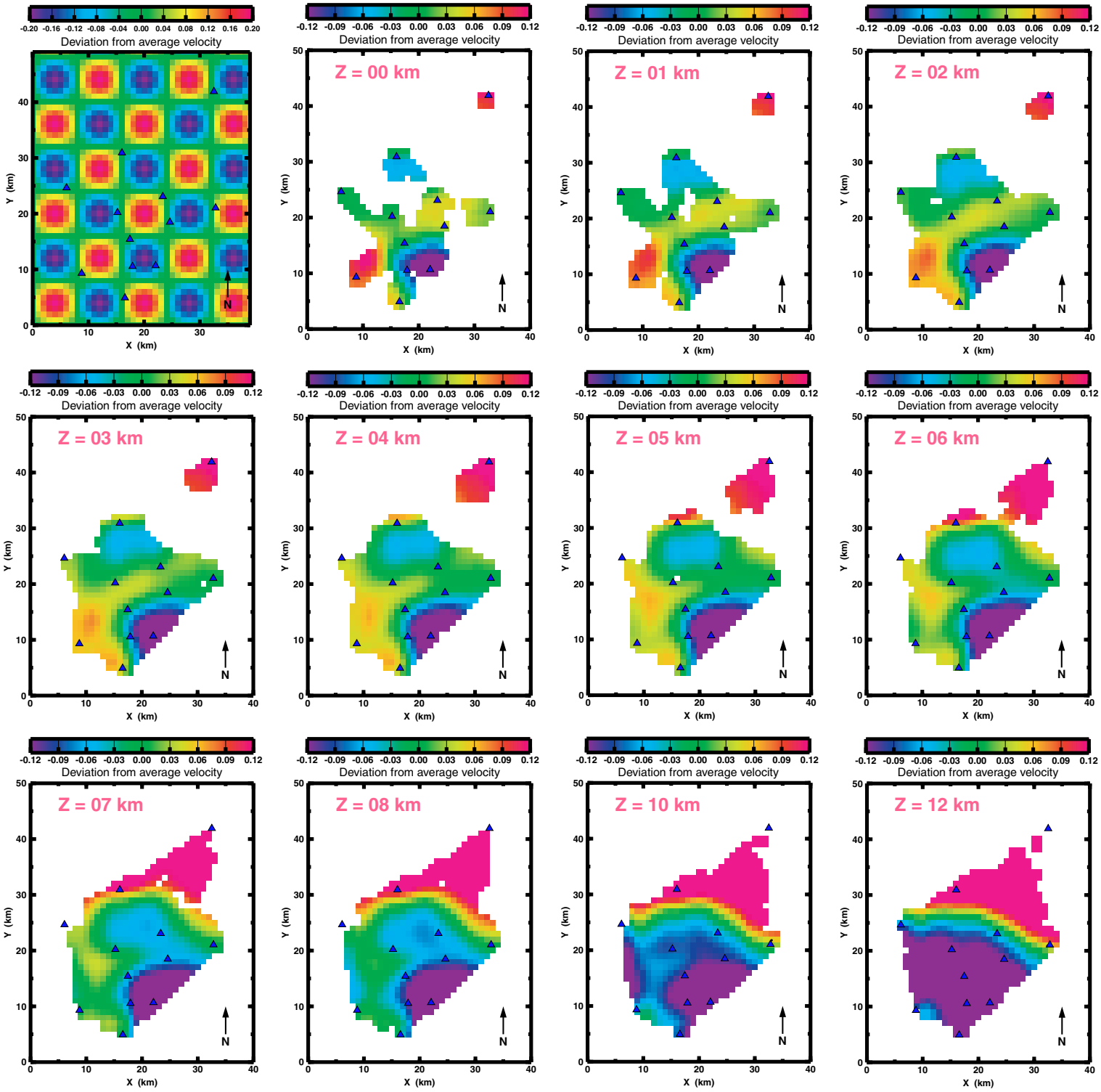

Figure A14. Depth slices through reconstructed 8 km checkerboard model (pattern configuration 1).

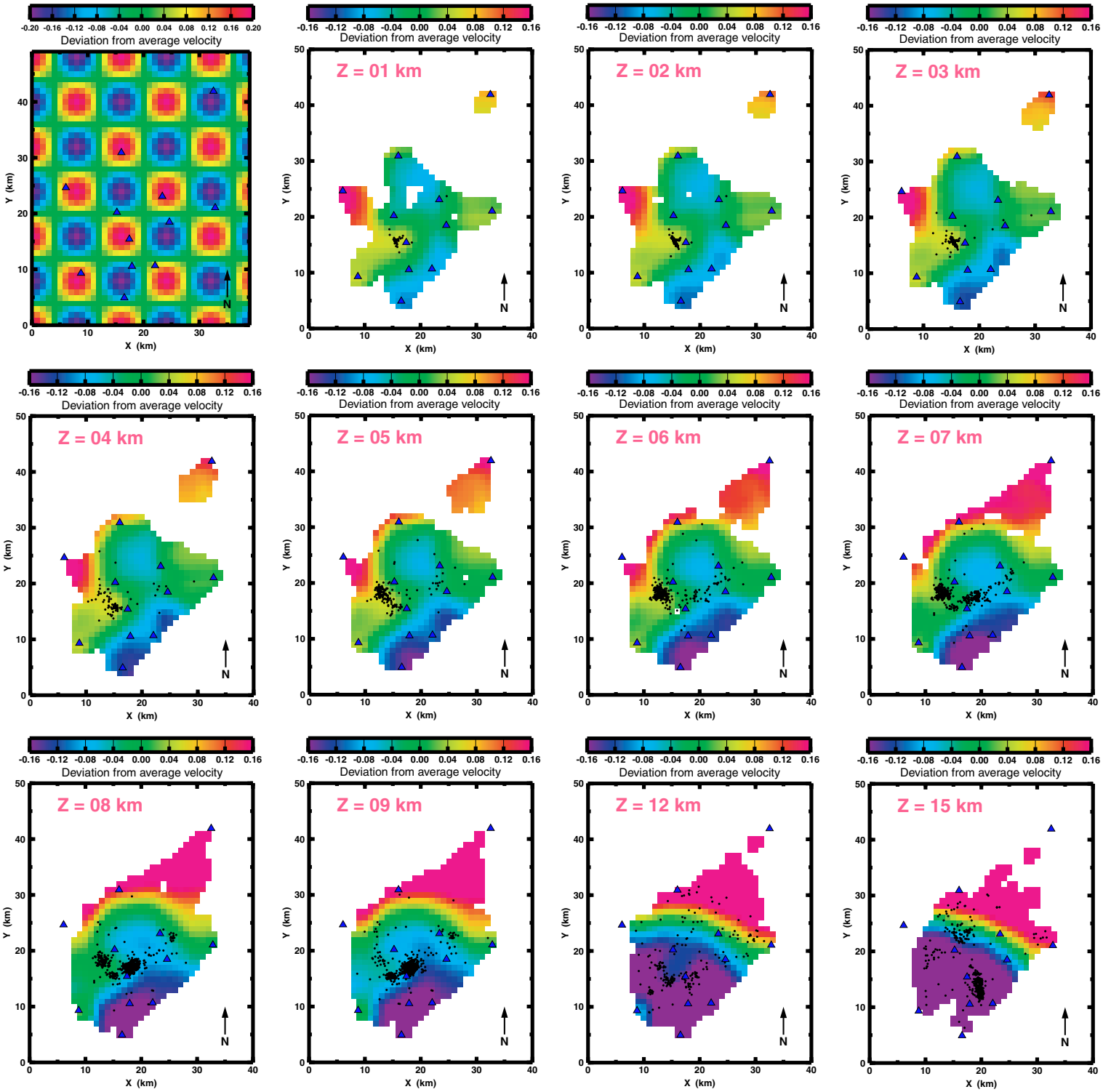

Figure A15. Depth slices through reconstructed 8 km checkerboard model (pattern configuration 2).

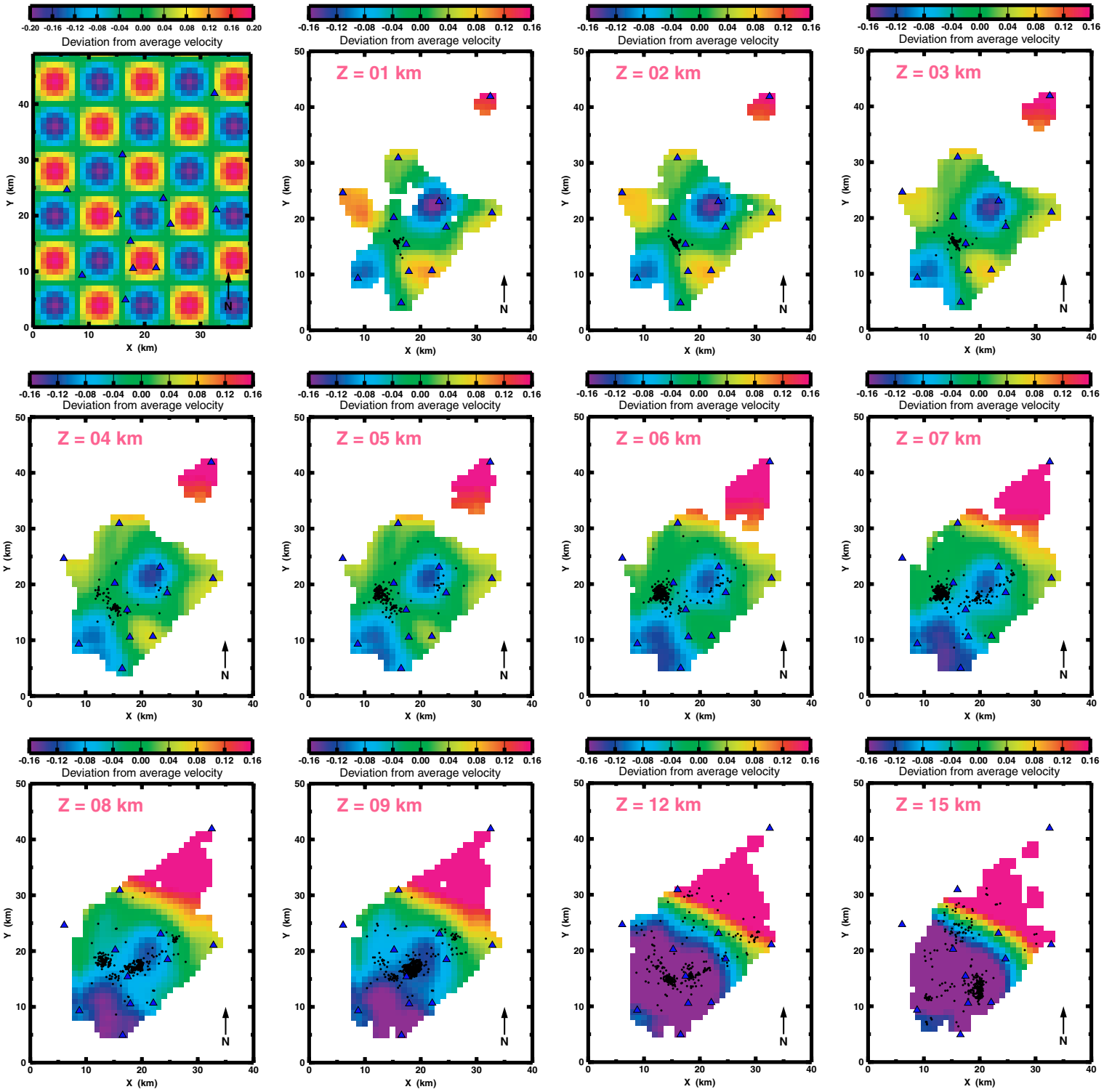

Figure A16. Depth slices through reconstructed 8 km checkerboard model (pattern configuration 3).

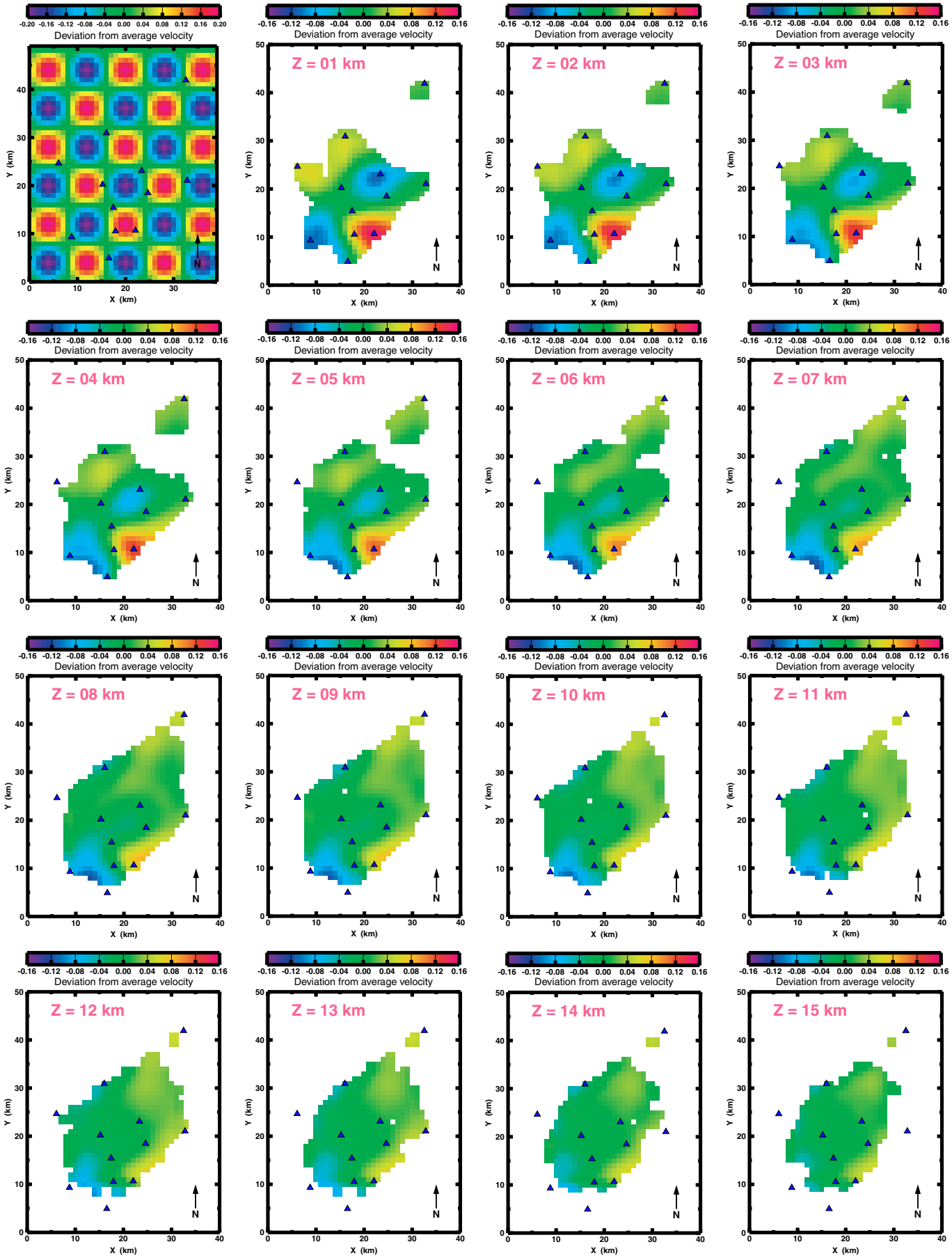

Figure A17. Depth slices through reconstructed 8 km checkerboard model (pattern configuration 4).

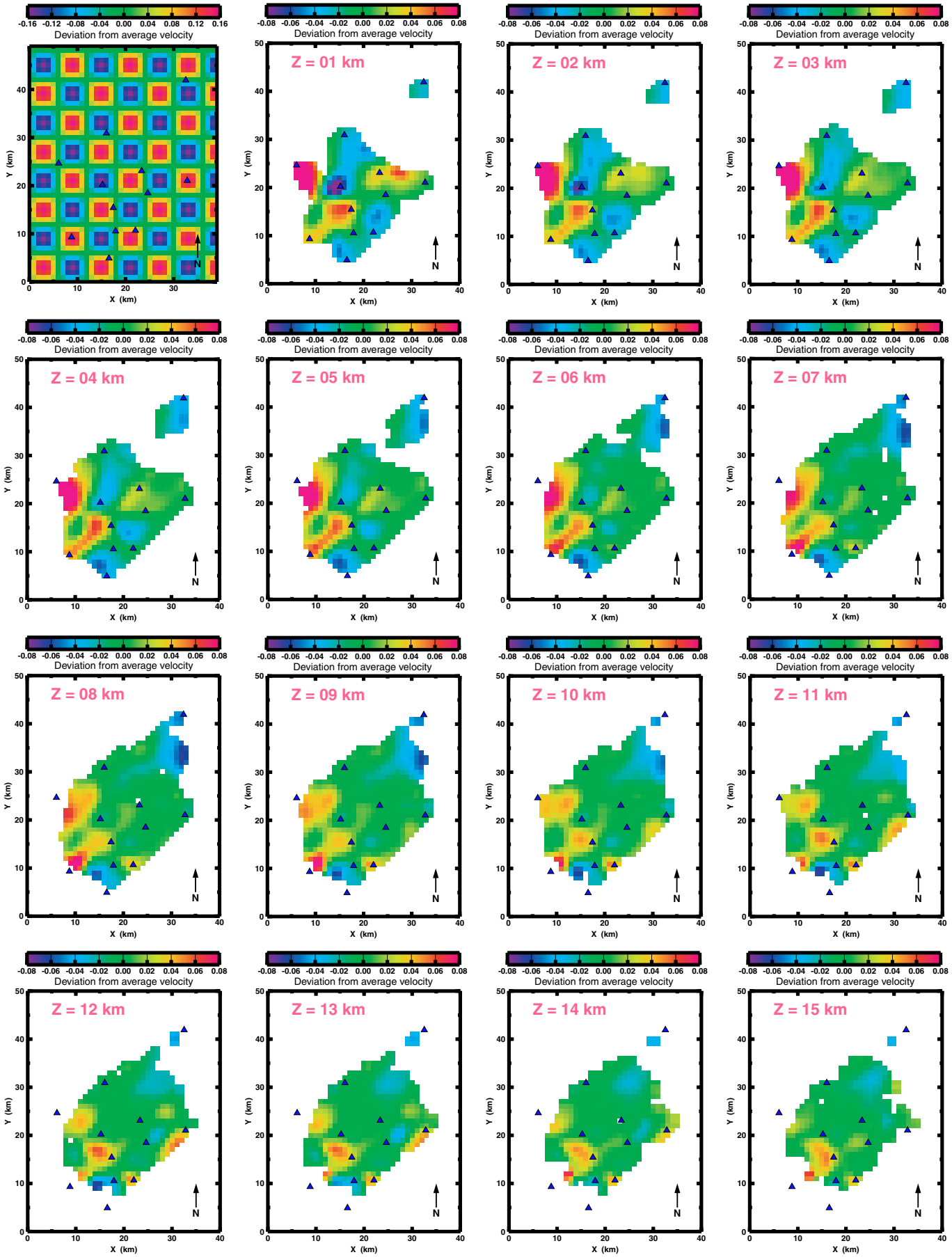

Figure A18. Depth slices through reconstructed 6 km checkerboard model (pattern configuration 1).

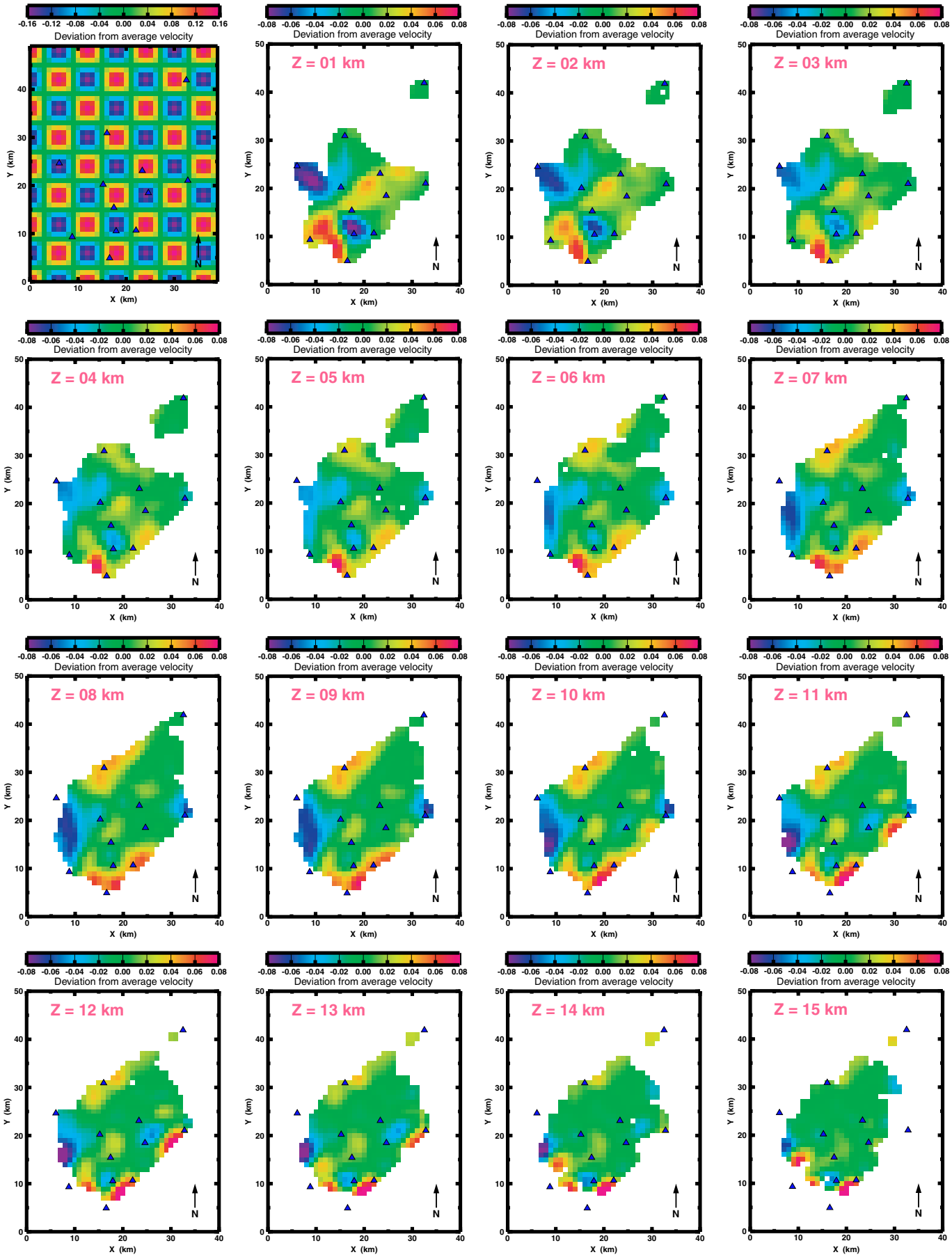

Figure A19. Depth slices through reconstructed 6 km checkerboard model (pattern configuration 2).

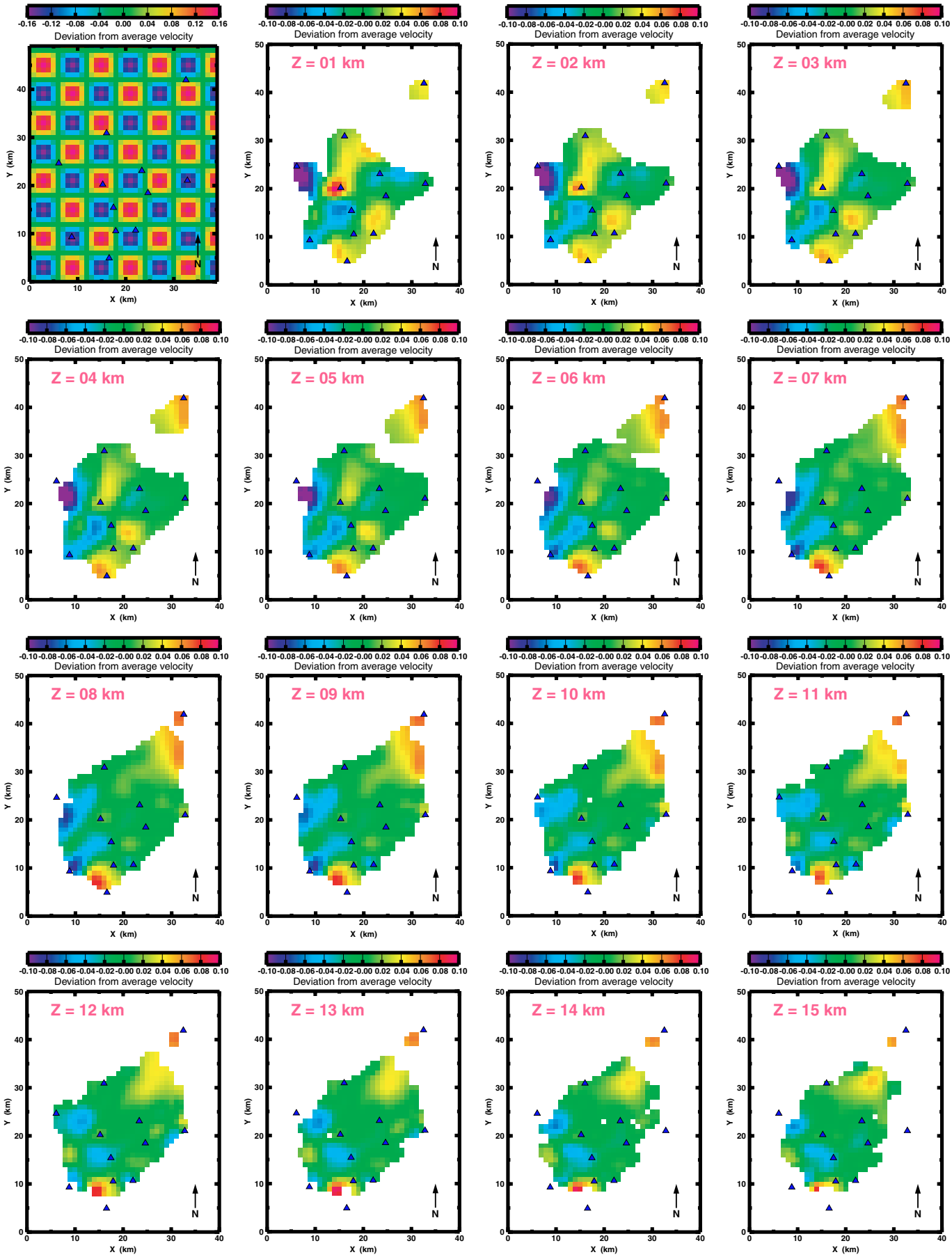

Figure A20. Depth slices through reconstructed 6 km checkerboard model (pattern configuration 3).

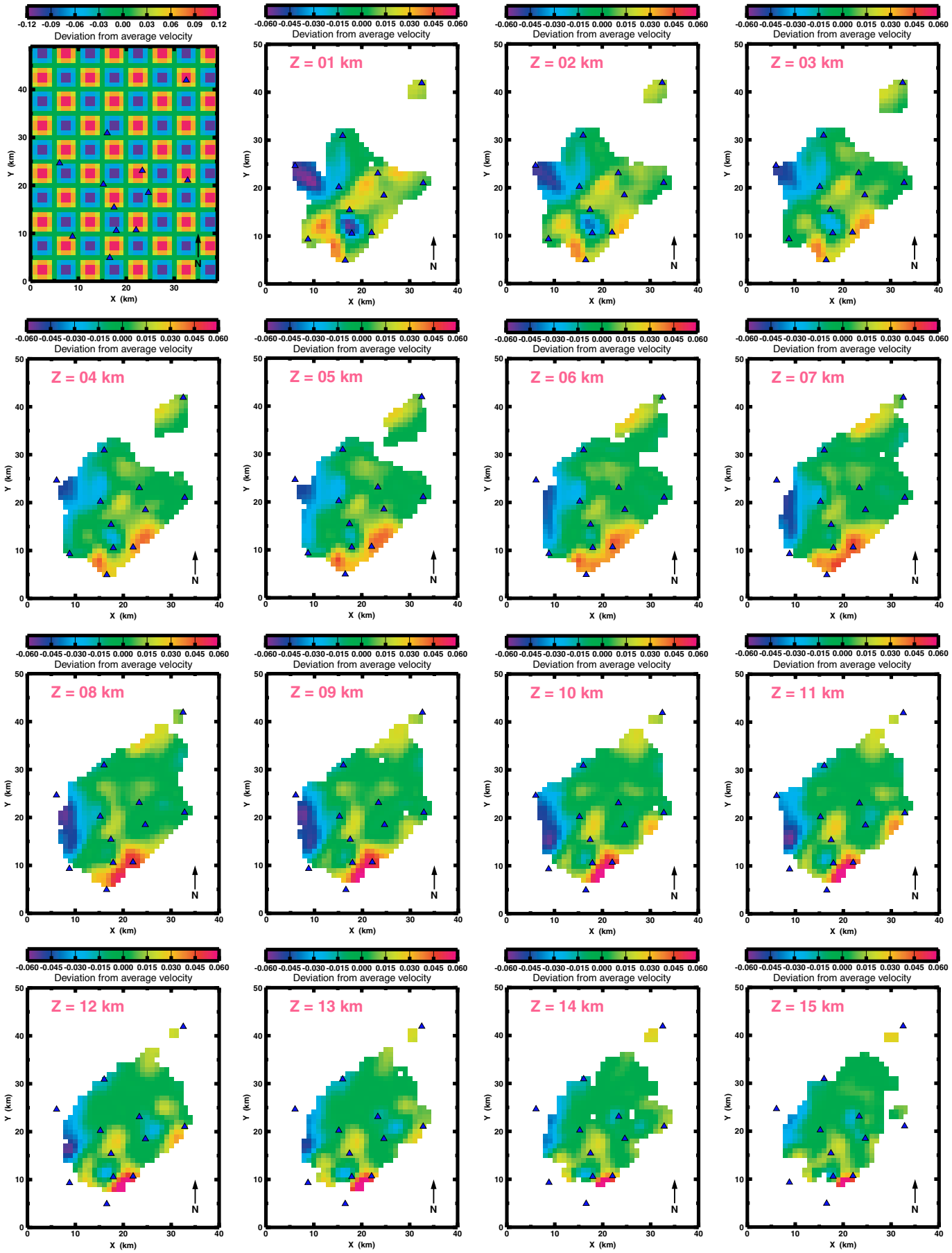

Figure A21. Depth slices through reconstructed 5 km checkerboard model (pattern configuration 1).

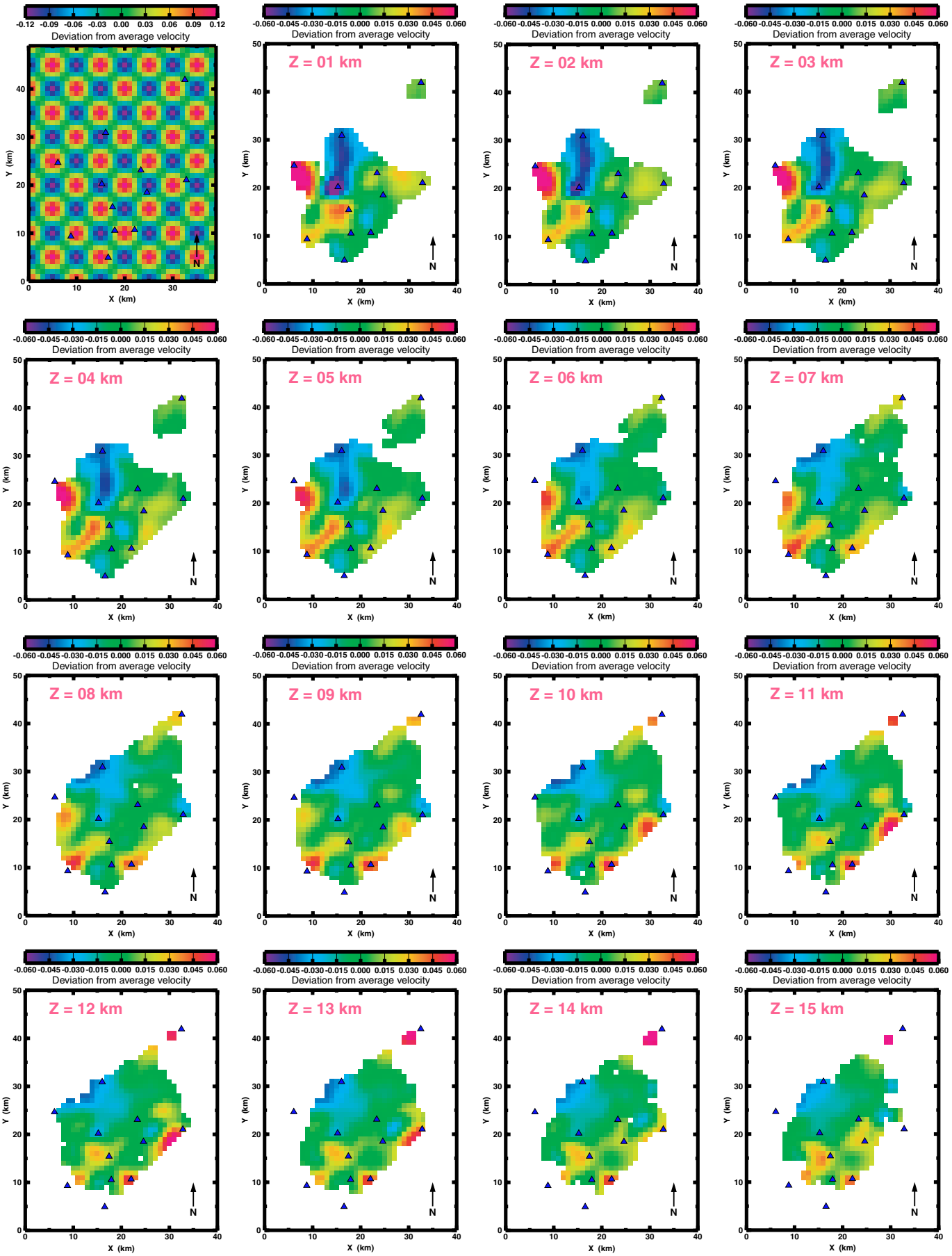

Figure A22. Depth slices through reconstructed 5 km checkerboard model (pattern configuration 2).

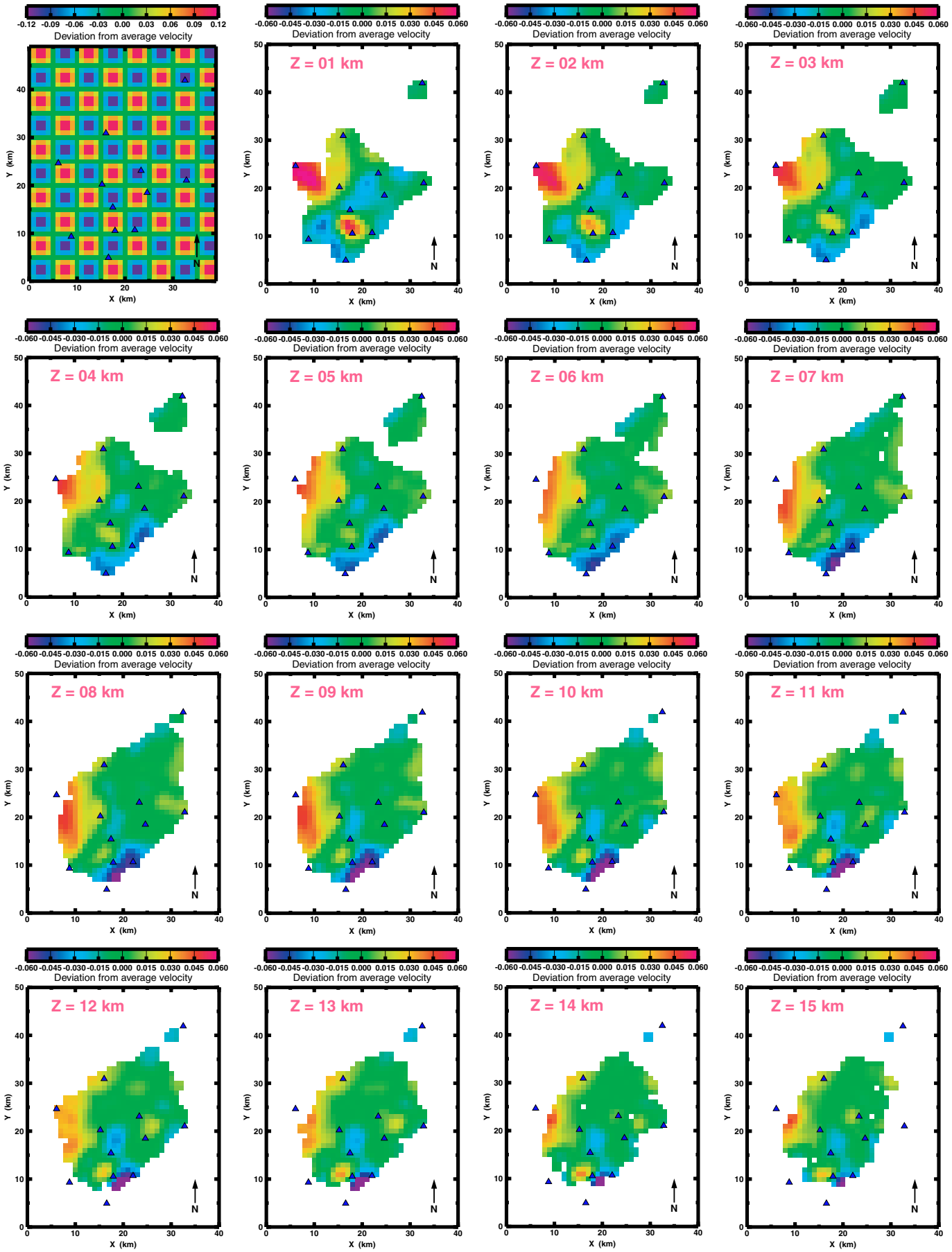

Figure A23. Depth slices through reconstructed 5 km checkerboard model (pattern configuration 3).

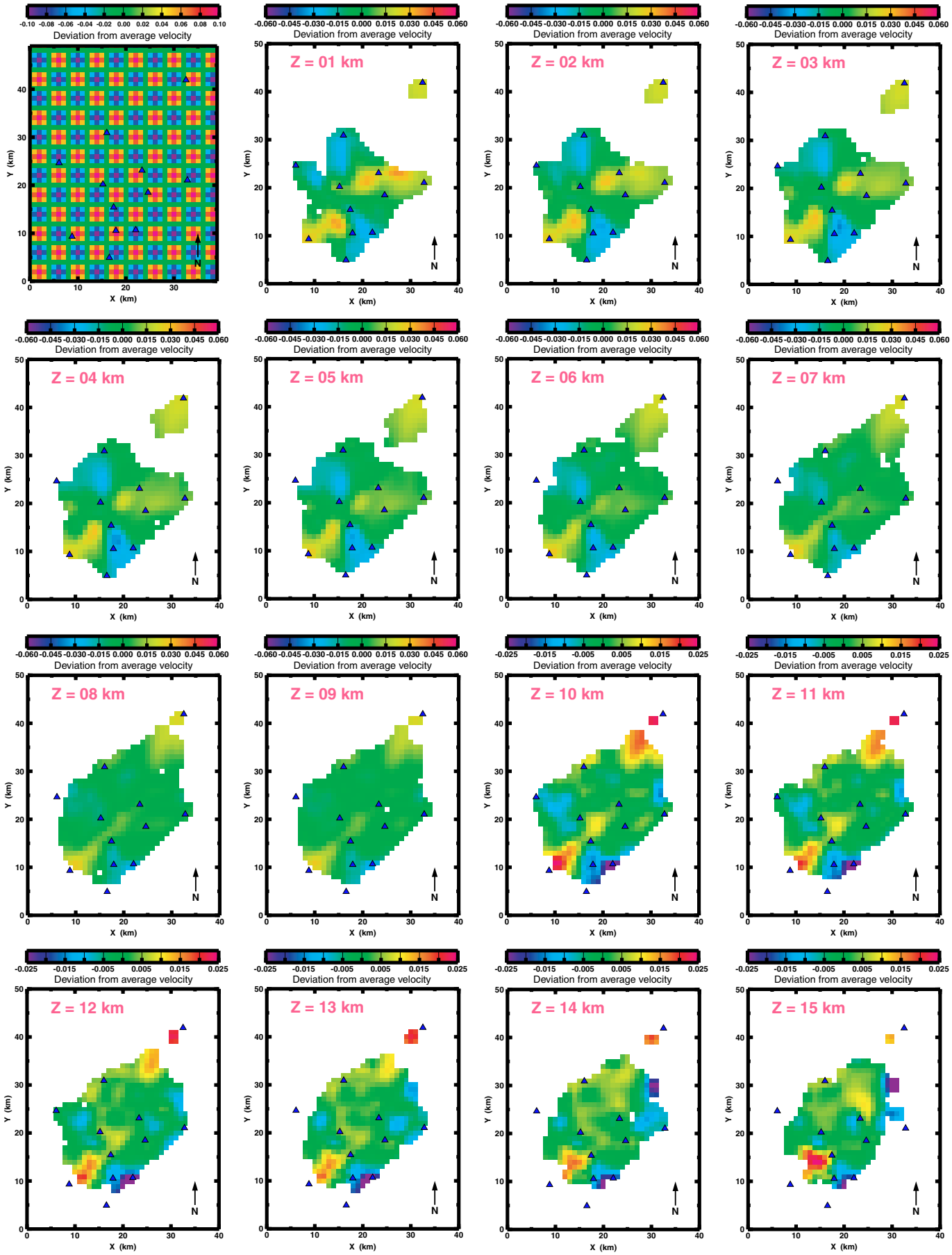

Figure A24. Depth slices through reconstructed 4 km checkerboard model (pattern configuration 1).

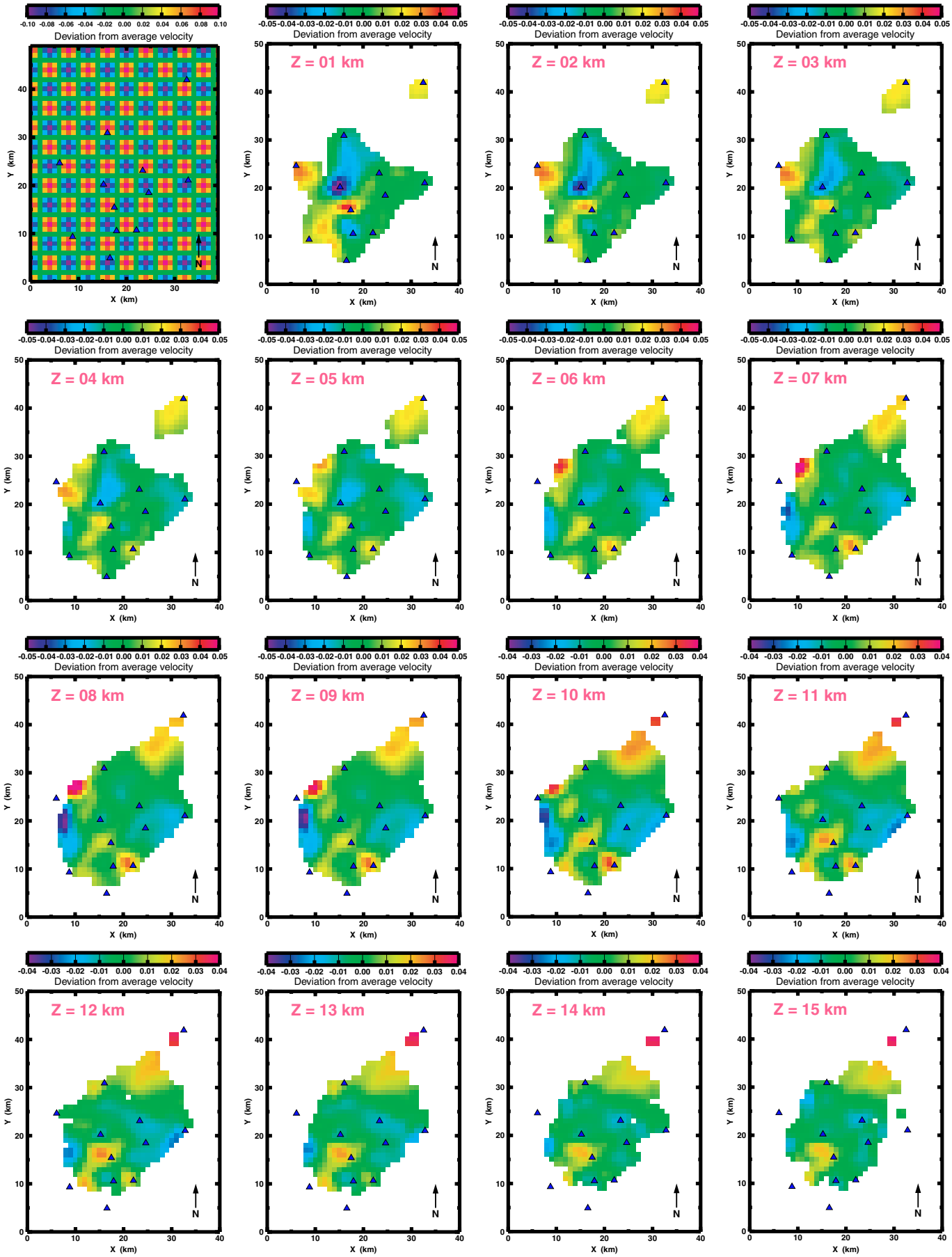

Figure A25. Depth slices through reconstructed 4 km checkerboard model (pattern configuration 2).

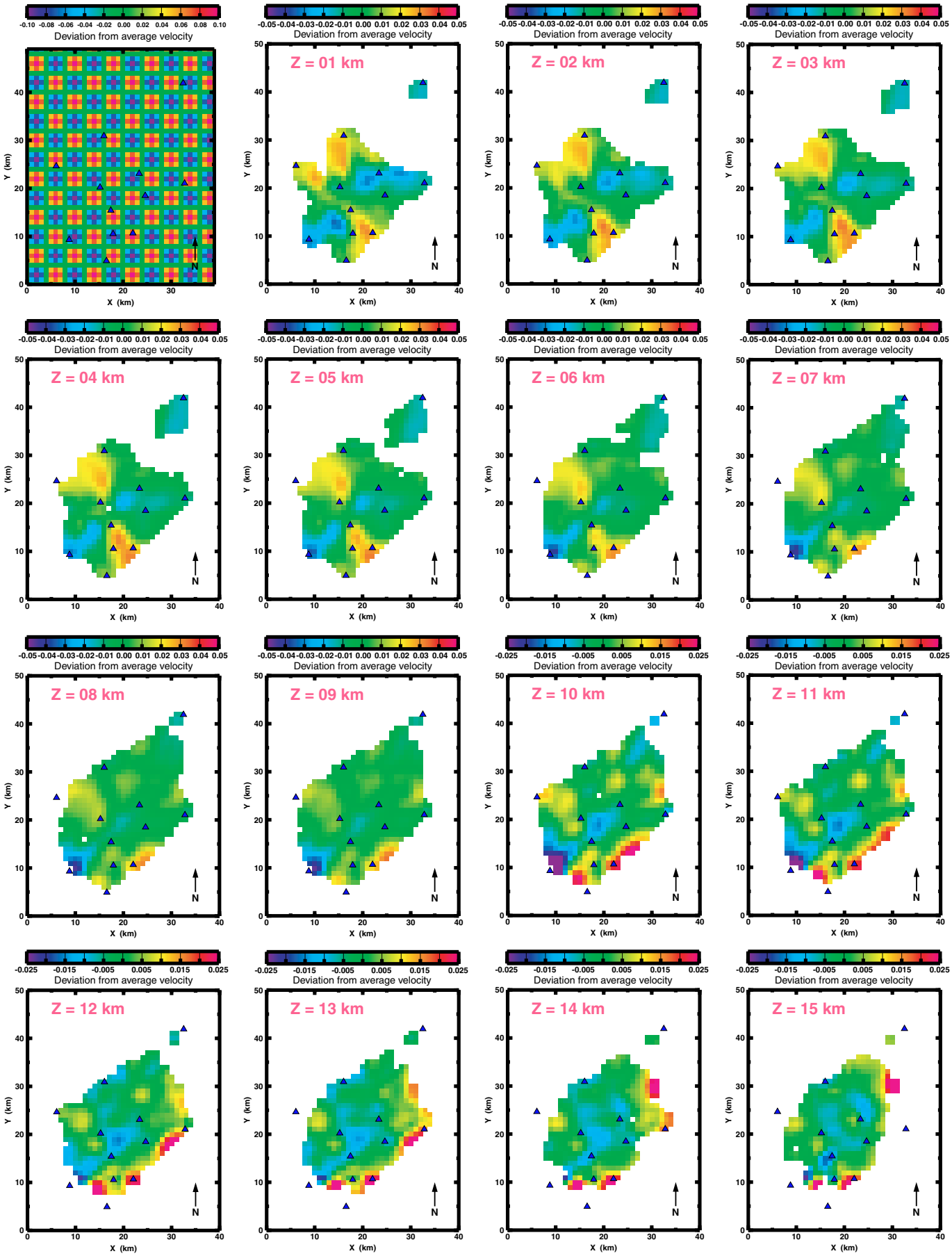

Figure A26. Depth slices through reconstructed 4 km checkerboard model (pattern configuration 3).

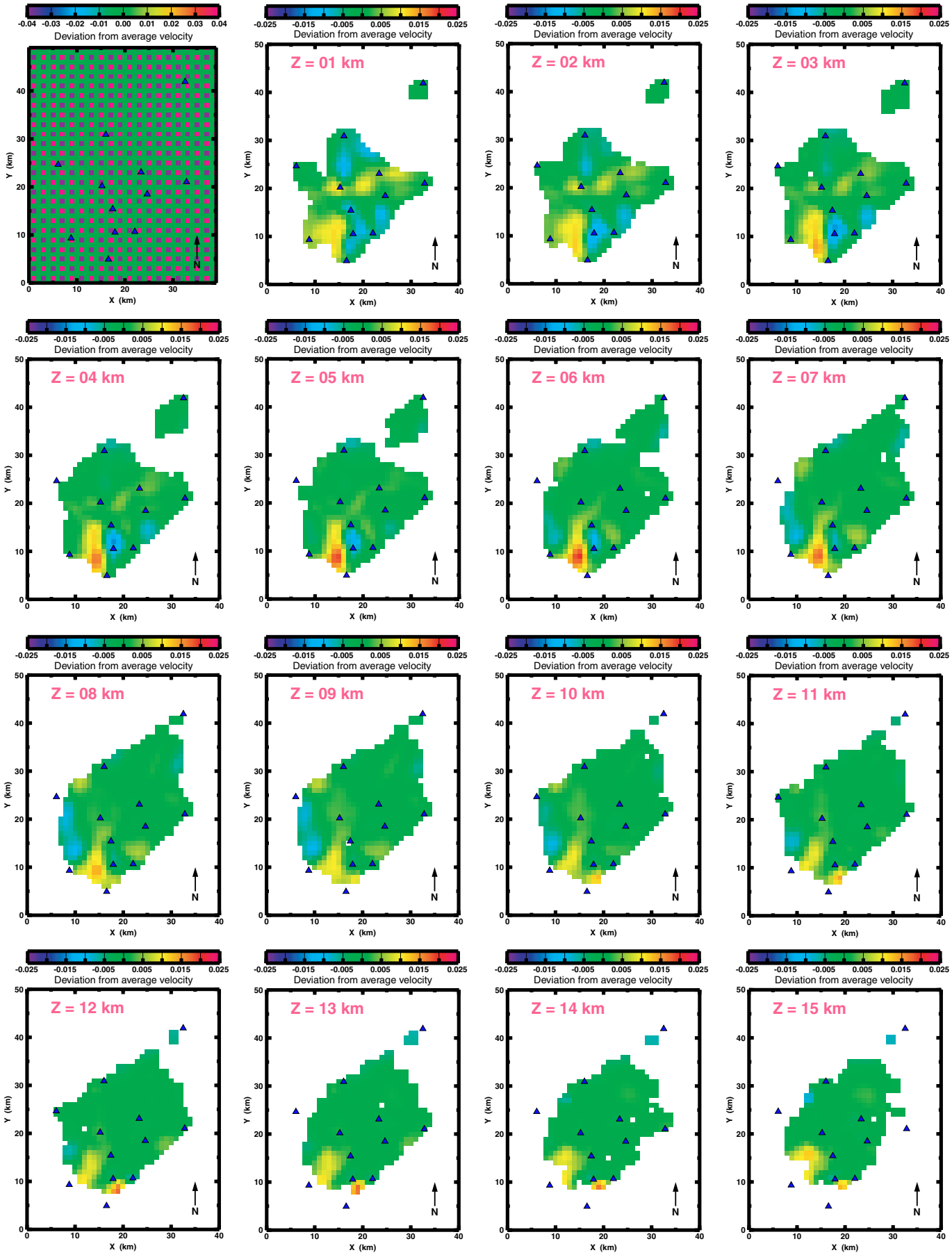

Figure A27. Depth slices through reconstructed 2 km checkerboard model.